Inhibition of JAK2V617F-Driven Neoplastic Endothelial Dysfunction by IFNα as a Novel Antifibrotic Mechanism

Madeline J. Caduc[1,2], Mohamed H. E. Mabrouk[3], Martin Grasshoff[4], Pia Wanner[5], Katrin Götz[5], Jessica E. Pritchard[5-7], Dickson W. L. Wong[8], Cristina B. Lopez[1,2], Louisa Böttcher[8], Pinar Sönmez[8], Bärbel Junge[1,2], Eva M. Buhl[8], Sabrina Ernst[9], Gerhard Müller-Newen[10], Michael Vogt[11], Jörg Eschweiler[12,13], Peter Boor[8], Maximilian Ackermann[8], Nicolas Chatain[1,2], Julia Franzen[3], Ivan G. Costa[4], Martin Zenke[1], Rebekka K. Schneider[5-7], Radek Skoda[14], Tim H. Brümmendorf[1,2], Steffen Koschmieder[1,2,15*], Marcelo A. S. de Toledo[1,2,15*]

1 Department of Hematology, Oncology, Hemostaseology and Stem Cell Transplantation, Faculty of Medicine, RWTH Aachen University, Aachen, Germany

2 Center for Integrated Oncology Aachen Bonn Cologne Düsseldorf (CIO ABCD), Aachen, Germany

3 Genomics Facility, Interdisciplinary Center for Clinical Research IZKF, RWTH Aachen University, Aachen, Germany

4 Institute for Computational Genomics, RWTH Aachen University, Aachen, Germany

5 Institute for Cell and Tumor Biology, RWTH Aachen University, Aachen, Germany

6 Department of Developmental Biology, Erasmus University Medical Center, Rotterdam, Netherlands

7 Oncode Institute, Erasmus University Medical Center Cancer Institute, Rotterdam, Netherlands

8 Institute of Pathology and Electron Microscopy Facility, RWTH Aachen University Hospital, Aachen, Germany

9 Confocal Microscopy Facility, Interdisciplinary Center for Clinical Research IZKF, Uniklinik RWTH Aachen, Aachen, Germany

10 Institute of Biochemistry and Molecular Biology, Uniklinik RWTH Aachen, Aachen, Germany

11 Two-Photon Imaging Facility, Interdisciplinary Center for Clinical Research IZKF, RWTH Aachen University Hospital, Aachen, Germany

12 Department of Trauma and Reconstructive Surgery, Faculty of Medicine, Martin-Luther-University Halle (Saale), Germany

13 Department of Trauma and Reconstructive Surgery, BG Klinikum Bergmannstrost Halle (Saale), Germany

14 Department of Biomedicine, Experimental Hematology, University Hospital Basel and University of Basel, Basel, Switzerland

15 Shared senior authorship

* Corresponding authors: Dr. Marcelo A. S. de Toledo, PhD, and Prof. Dr. med. Steffen Koschmieder, Department of Hematology, Oncology, Hemostaseology, and Stem Cell Transplantation, Faculty of Medicine, RWTH Aachen University, Pauwelsstr. 30, D-52074 Aachen, Germany, Phone: +49-241-8036102; E-mail: mszymanskide@ukaachen.de and skoschmieder@ukaachen.de

Bullet Points

- Arterial vascular remodeling emerges as a novel hallmark of MPN, characterized by TNFα-inflammation, ribosomal dysregulation and EndMT.
- IFNα restores neoplastic endothelial dysfunction, highlighting its role as a vascular niche-modulating and anti-fibrotic agent in MPN.

Abstract

The vascular niche is a critical regulator of hematopoiesis and disease progression in myeloproliferative neoplasms (MPN). The presence of JAK2V617F+ endothelial cells (EC) in MPN patients and their association with cardiovascular complications highlight the need to understand and therapeutically target this compartment. Using patient-specific induced pluripotent stem cells (iPSC) harboring $JAK2^{WT}$ or the MPN-driver JAK2V617F (heterozygous, $JAK2V617F^{HET}$, or homozygous, $JAK2V617F^{HOM}$), we identified zygosity-dependent transcriptional profiles in iPSC-derived EC (iEC) at baseline and following interferon-alpha (IFNα) treatment. $JAK2V617F^{HET}$ iEC exhibited an endothelial-to-mesenchymal transition (EndMT) signature, while $JAK2V617F^{HOM}$ iEC showed suppression of translation and ribosome biogenesis. Leveraging iPSC-based 3D assembloids that mimic the bone marrow (BM) niche, we showed that JAK2V617F-driven EndMT is inhibited by tyrosine kinase inhibitors and IFNα. In both JAK2V617F-driven polycythemia vera and TPO-driven myelofibrosis murine models, scRNA-seq analysis of the BM vascular niche consistently revealed inflammatory and EndMT-associated signatures in arterial and arteriolar EC. Notably, dysregulation of ribosome- and translation-related pathways emerged in the myelofibrosis model and at advanced disease stages in JAK2V617F-driven polycythemia vera, indicating progressive vascular remodeling with disease evolution. Chronic pegylated IFNα treatment *in vivo* effectively reversed these pathological changes. IFNα's anti-EndMT activity was further validated in BM biopsies from MPN patients undergoing IFNα therapy. This is the first study to define MPN stage-dependent vascular remodeling and zygosity-specific endothelial effects of JAK2V617F, and to directly link IFNα-mediated EndMT inhibition as a novel antifibrotic mechanism. Our 3D assembloids provide a translational platform for mechanistic studies and therapeutic targeting of the BM microenvironment in MPN.

Introduction

Myelofibrosis (MF) represents an advanced stage of BCR:ABL1-negative myeloproliferative neoplasms (MPN), marked by progressive bone marrow (BM) fibrosis that impairs normal hematopoiesis and promotes inflammatory and vascular complications[1]. Disruption of the vascular niche, including aberrant neoangiogenesis[2,3] and endothelial-to-mesenchymal transition (EndMT)[4], has been observed in MPN progression[5] and cardiovascular dysfunction (CVD)[6]. While the pathogenesis of cardiovascular complications in MPN remains debated, the detection of JAK2V617F+ endothelial cells (EC) in patients and multilineage analyses suggest that these clonal hematologic malignancies may originate from a common precursor, the hemangioblast [7–10].

Clinically, in MPN, interferon-alpha (IFNα) induces hematologic and molecular responses and, potentially, delay of fibrotic progression[11,12]. In addition to its antiproliferative and immunomodulatory effects, IFNα also exhibits antitumor properties through inhibition of angiogenesis[13]. While previous studies have described its transcriptional effects on EC[14], the impact of IFNα on the malignant clone-associated microenvironment, particularly the JAK2V617F+ vascular niche, remains largely unexplored.

Induced pluripotent stem cell (iPSC)-derived organoids and assembloids offer a robust platform for modeling hematologic diseases and drug screening, faithfully recapitulating tissue architecture, cellular composition, and patient-specific genetics *in vitro*[15,16]. In this study, we conducted global transcriptomic profiling of MPN patient-derived iPSC-endothelial cells (iEC) to uncover zygosity-specific transcriptional programs and distinct responses to IFNα treatment. To further dissect the neoplastic vascular niche and its modulation by IFNα, we employed single-cell RNA sequencing (scRNA-seq) of complex iPSC-derived assembloids composed of wild-type or

167 JAK2V617F+ endothelial and hematopoietic cells. These *in vitro* findings were
168 complemented by *in vivo* analyses using two distinct murine MPN models: a
169 JAK2V617F-driven polycythemia vera (PV) model and a thrombopoietin (TPO)
170 overexpression model that recapitulates advanced MF. Both models included
171 treatment with pegylated IFNα (pIFNα) or vehicle to evaluate EndMT and
172 microenvironmental transcriptomic remodeling at single-cell resolution. Finally, the
173 anti-EndMT activity of pIFNα was validated in BM biopsies from MPN patients
174 undergoing pIFNα therapy.

175 We provide the first evidence of IFNα-mediated regulation of neoplastic
176 endothelial dysfunction in MPN across both human and murine disease models, as
177 well as patient material. Moreover, our 3D *ex vivo* model provides a physiologically
178 relevant platform to dissect cellular crosstalk underlying MF pathogenesis and to
179 evaluate therapeutic effects on the BM niche.

180

181 **Methods**

182 **Ethics Approval and Consent to Participate**

183 Peripheral blood mononuclear cells from MPN patients were obtained from the
184 centralized Biomaterial Bank of the Faculty of Medicine, RWTH Aachen University
185 Medical Center. The mesenchymal stromal cells (MSC) used in this study were isolated
186 from the femoral heads of patients undergoing hip replacement surgery (Department
187 of Orthopedics, Trauma and Reconstructive Surgery, Faculty of Medicine, RWTH
188 Aachen University). All biological samples were obtained after written informed
189 consent, as approved by the Ethics Committee of the RWTH Aachen University
190 (EK206/09, EK127/12, EK300/13). Murine experiments were conducted in accordance
191 with institutional guidelines and approved by the relevant ethics committee (81-
192 02.04.2019.A380).

193 **Differentiation of MPN Patient-Specific iPSC Towards Endothelial and**
194 **Hematopoietic Lineages**

195 The iPSC lines used in this study were previously characterized[17,18] and are listed in
196 Supplemental Table 1. Differentiation into hematopoietic and endothelial lineages
197 followed established protocols[19–21].

198

199 **Generation of 3D Fibrin-Based Assembloids**

200 Fibrin hydrogels were generated as previously described[22,23], with compositions
201 detailed in Supplemental Table 2. Detailed protocols for the 3D experimental setups
202 are provided in the Supplemental Methods.

203

204 **MPN Murine Models**

205 The JAK2V617F-driven PV model and TPO-overexpression model of MF have been
206 described previously[24,25]. Detailed methods are provided in the Supplemental
207 Methods.

208

209 **Statistical Analysis**

210 Graphical display and statistical analysis were performed with Prism (GraphPad, San
211 Diego, CA, USA). P values of <0.05 were considered statistically significant. Results
212 are presented as mean ± standard deviation (*p < 0.05, **p < 0.01, ***p < 0.001).

213

214 **Additional Experimental Procedures**

215 The Supplemental Methods include detailed protocols for iPSC differentiation,
216 generation of iPSC-based assembloids, proliferation and apoptosis assays, *in vitro*
217 drug screening, confocal and transmission electron microscopy, and validation studies
218 using MPN murine models and human BM trephines. Additional protocols for

219 immunofluorescence, flow cytometry, bulk and single-cell RNA sequencing, RT-qPCR,
220 and associated reagents are provided, including IF antibodies (Supplemental Table 3),
221 primers (Supplemental Table 4), FACS antibodies (Supplemental Table 5), compounds
222 (Supplemental Table 6), and media compositions.
223

224 ## Results

225 **JAK2V617F Zygosity Shapes Transcriptional Programs in iEC at Baseline and**
226 **Following IFNα Treatment**

227 To investigate the impact of JAK2V617F on human vasculogenesis, we utilized
228 high-purity (97.13±3.27%) clonal patient-specific $JAK2^{WT}$ and JAK2V617F+
229 CD31+CD144+CD105+ iEC (Supplemental Fig. 1A). While JAK2V617F did not affect
230 endothelial differentiation, angiogenic potential, or viability in response to drugs used
231 or under investigation for MPN, including IFNα, it conferred a proliferative advantage
232 to iEC (Supplemental Fig. 1B-E). Acute IFNα exposure did not affect capillary-like
233 structure formation, whereas pre-sensitization markedly impaired angiogenesis, with
234 no additional effect upon re-exposure (Supplemental Fig. 1F–J).

235 In global RNA-seq analysis, unsupervised clustering of differentially expressed
236 genes (DEG) segregated samples by JAK2V617F zygosity (Fig. 1A), while JAK2 and
237 STAT1 gene expression levels remained comparable across genotypes (Supplemental
238 Fig. 2A-B, Supplemental Tables 7, 8).

239 Upon IFNα treatment, iEC showed a robust interferon response, with
240 upregulation of antiviral and immunomodulatory pathways (Fig. 1B; Supplemental
241 Fig. 2C). Key interferon-stimulated genes (*IFIT1*, *STAT1*, *USP18*) were validated by
242 RT-qPCR (Supplemental Fig. 2D). IFNα treatment did not induce apoptosis
243 (Supplemental Fig. 2E–F), consistent with drug screening results showing preserved

244 iEC viability after 72 hours treatment (Supplemental Fig. 1E). PROGENy analysis[26]
245 confirmed similar JAK–STAT activation across genotypes (Supplemental Fig. 2G).
246 Differential expression analysis revealed zygosity-dependent transcriptional
247 alterations both at baseline and following IFNα treatment. At baseline, JAK2V617F^{HOM}
248 iEC exhibited downregulation of translation- and ribosome-associated gene sets
249 (Fig. 1C), including ribosomal regulatory non-coding RNA (ncRNA) such as
250 SNORA73B (Fig. 1D; Supplemental Fig. 3A)[27]. Disruption of pathways related to
251 ribosome biogenesis, ribonucleoprotein complex assembly, and RNA splicing was also
252 observed (Supplemental Fig. 3B). Consistently, transmission electron microscopy
253 (TEM) revealed disorganized ER–ribosome architecture and reduced rough ER (rER)
254 in homozygous iEC (Fig. 1E; Supplemental Fig. 3C; Supplemental Table 9). Following
255 IFNα treatment, JAK2V617F^{HOM} iEC displayed the highest number of uniquely
256 regulated DEG (Supplemental Table 10), including restoration of ncRNA (Fig. 1F)[28,29],
257 and enrichment of ribosome biogenesis and mRNA splicing pathways (Fig. 1G). This
258 effect was not observed in JAK2^{WT} controls (Supplemental Fig. 3D).
259 In JAK2V617F^{HET} iEC, gene set enrichment analysis (GSEA) identified
260 upregulation of TGFβ signaling and EMT-associated genes (Fig. 1H), along with
261 enrichment of hypoxia and reactive oxygen species (ROS)-related genes
262 (Supplemental Fig. 3E), both shown to be critical for MPN pathogenesis[30,31]. Pathways
263 involved in mesenchymal development, and extracellular matrix (ECM) synthesis were
264 also upregulated (Supplemental Fig. 3F). Concordantly, expression of key EndMT
265 markers such as fibroblast-specific protein 1 (FSP1) and α-smooth muscle actin
266 (ACTA2) was increased in JAK2V617F$^{HET\ vs.\ WT}$ iEC (Fig. 1I; Supplemental Fig. 3G-
267 H)[32].
268 These findings demonstrate that JAK2V617F zygosity drives distinct
269 transcriptional programs in iEC which can be reversed by IFNα treatment.

270

271 **IFNα and Tyrosine Kinase Inhibitors Mitigate the Pro-Fibrotic Phenotype of**
272 **JAK2V617F^{HET} iEC**

273 Tyrosine kinase inhibitors like ruxolitinib and nintedanib exert anti-fibrotic
274 effects, including EndMT suppression[33–35], yet the mechanisms underlying IFNα's
275 disease-modifying properties remain unclear[36]. Given the pro-mesenchymal signature
276 observed in JAK2V617F^{HET} iEC, we investigated their contribution in BM niche fibrosis
277 and IFNα's capacity to counteract EndMT. Ruxolitinib served as a positive control,
278 while nintedanib, an emerging agent in hematologic disorders[37], was tested alone and
279 in combination with ruxolitinib to assess potential synergy.

280 We developed 3D fibrin-based assembloids that mimic critical EC-MSC
281 interactions required for vessel formation[38] (Fig. 2A). iEC formed vessel-like structures,
282 enhanced by MSC, and the model recapitulated our initial endothelial tube formation
283 assay findings, including the anti-angiogenic impact of IFNα pre-sensitization
284 (Supplemental Fig. 4A–C).

285 Consistent with the pro-mesenchymal transcriptional signature, JAK2V617F^{HET}
286 cocultures showed elevated FSP1 protein levels, both overall and iEC-specific,
287 compared to WT (Fig. 2B–C). Exposure of assembloids to pro-inflammatory and pro-
288 fibrotic cytokines (TGFβ, IL-1β, and TNFα) induced features of myelofibrotic
289 transformation, including increased collagen I (Col1a1) and αSMA deposition (Fig. 2D,
290 Supplemental Fig. 4D). A mesenchymal shift in iEC was confirmed in 2D cultures, with
291 JAK2V617F^{HET} iEC exhibiting reduced *CLDN5* expression and cytokine-induced
292 upregulation of *SNAI1* alongside downregulation of *CD31* (Supplemental Fig. 4E).

293 Nintedanib, ruxolitinib, and their combination significantly reduced overall and
294 iEC-specific FSP1 protein deposition in JAK2^{WT} and JAK2V617F^{HET} assembloids (Fig.
295 2E–G), while IFNα induced a trend toward reduction (Fig. 2G). This reduction was

296 associated with decreased Col1a1 and αSMA deposition, while CD31 expression
297 remained unchanged across all conditions, indicating preserved vascular integrity (Fig.
298 2H–I, Supplemental Fig. 4F).
299 These findings suggest that IFNα and, ruxolitinib and nintedanib, have the
300 potential to suppress EndMT.
301
302 **iPSC-Based Assembloids Mimic Key Cellular Interactions of the Human BM**
303 **Niche**
304 To better replicate *in vivo* conditions and further investigate the role of mutant
305 endothelium and impact of IFNα treatment on BM niche remodeling, we incorporated
306 hematopoietic cells ($JAK2^{WT}$ or $JAK2V617F^{HET}$ iHC) into our assembloids. These
307 included $CD117^{+}CD34^{+}$ hematopoietic stem/progenitor cells,
308 $CD45^{+}CD61/41^{+}$megakaryocytes, $CD45^{+}CD68^{+}$ monocytes/macrophages, and
309 $CD45^{+}CD66b^{+}$ granulocytes (Fig. 3A, Supplemental Fig. 5A). scRNAseq of these
310 complex 3D assembloids identified distinct hematopoietic populations based on
311 transcriptional profiles and lineage-defining marker expression (Fig. 3B). Within the
312 non-hematopoietic ($CD45^{-}$) compartment, eight distinct clusters were identified: six
313 mesenchymal, one endothelial, and one hemogenic endothelial cluster (Supplemental
314 Fig. 5B, Supplemental Table 11).
315 We first analyzed scRNA-seq data from unmutated 3D assembloids to map
316 functional crosstalk between cellular subtypes, revealing extensive autocrine and
317 paracrine signaling between stromal and hematopoietic compartments (Fig. 3C).
318 Stromal cells, including EC, and basophil progenitors emerged as primary sources of
319 outgoing signals, engaging in ECM- and growth factor–mediated interactions via
320 ligands such as collagen, laminin, VEGF, PDGF, and KIT (Fig. 3D). Predicted ligand–
321 receptor (L–R) interactions included *ANGPT1/2–TEK*, *KIT–KITL*, *CXCL12–CXCR4*,

322 and *JAG1–NOTCH1*, underscoring the stromal compartment's central role in
323 supporting BM niche structure and function (Supplemental Fig. 5D).
324 Together, these findings highlight the transcriptional homology of our
325 assembloids with the human BM niche.
326
327 **JAK2V617F Drives Neoplastic Angiogenesis and Dysregulates Cellular**
328 **Crosstalk in 3D Assembloids**
329 Next, we examined JAK2V617F-driven transcriptional changes, focusing on its
330 effects in EC alone versus in combination with hematopoietic expression. Consistent
331 with our 2D data (Supplemental Fig. 1B), assembloids with JAK2V617F^{HET}
332 endothelium showed a significant increase in EC numbers, which was further amplified
333 by the presence of JAK2V617F^{HET} iHC (Fig. 4A). Mutated iEC exhibited a pro-
334 mesenchymal transcriptional profile, with increased expression of EndMT markers
335 such as *ACTA2*, *FSP1 (S100A4)*, and *FAP* (Fig. 4B), recapitulating our bulk RNA-seq
336 findings (Supplemental Fig. 6A). In assembloids harboring both mutated endothelium
337 and hematopoietic cells, *DEPP1*, *ACTA2*, and *SNAI1* were further upregulated, along
338 with glycolysis-associated genes (*MYC*, *LDH*, *GAPDH*), indicating advanced EndMT
339 (Fig. 4B; Supplemental Fig. 6B)[39].
340 While vascular-restricted JAK2V617F^{HET} reduced the strength of EC
341 interactions with niche components (Supplemental Fig. 6C), particularly via *COL4A1/2*
342 and *CALM1*, basophil progenitors exhibited enhanced FN1 signaling through *ITGAV*
343 and *CD44* and stronger interactions with neutrophils, mast cells, and stromal cells via
344 the *SPP1–CD44* axis. Elevated SPP1, CD44, and FN1 are associated with poor cancer
345 prognosis due to their role in tumor microenvironment remodeling[40,41].
346 In JAK2V617F$^{HET\ vs.\ WT}$ assembloids, L–R interaction mapping revealed globally
347 increased cellular crosstalk, driven primarily by basophil progenitors and stromal

348 compartments including pericytes: aberrant signaling involved ECM components (e.g.,
349 collagen, FN1), angiogenic factors (e.g., PDGF, VEGF, ANGPTL), and inflammatory
350 mediators such as TGFβ (Fig. 4C–D). Additionally, increased interactions were
351 identified between hematopoietic progenitors, megakaryocytes, and EC with basophil
352 progenitors via the *MIF-CD74* axis (Supplemental Fig. 6D), a pathway implicated in
353 MPN development[42]. Moreover, basophil progenitors showed enhanced autocrine and
354 paracrine signaling with megakaryocytes and monocytes via the *LGALS1–ITGB1* axis
355 (Supplemental Fig. 6E), a pro-inflammatory pathway implicated in MF[43].

356 PROGENy analysis showed that the presence of JAK2V617F in both
357 endothelial and hematopoietic lineages markedly upregulated hypoxic signaling (Fig.
358 4E), a hallmark of MPN[31]. Cell types involved in fibrotic remodeling, including
359 monocytes/macrophages, neutrophils, MSC, and mast cells[37,44,45], exhibited robust
360 activation of the pro-inflammatory JAK-STAT pathway. The TGFβ pathway, a key driver
361 of fibrosis[46], was activated in MSC populations, mast cells, and monocytes (Fig. 4E).
362 Notably, IFNα and TNFα signaling were suppressed in MSC clusters (1, 5, and 6),
363 whereas hematopoietic cells showed enriched IFNα signaling (Fig. 4E).

364 Given the key role of the mesenchymal compartment in MF[44,47], we focused our
365 analysis on the JAK2V617F-driven transcriptional changes in the $CD45^{-}$ populations:
366 MAPK signaling, associated with fibrosis and carcinogenesis[48], was upregulated in EC
367 (cluster 4) and proliferative MSC (cluster 6), while pericytes (cluster 7) showed
368 enhanced PI3K activation. TGFβ signaling and ECM-related gene expression were
369 selectively enriched in MSC from mutated assembloids, whereas vascular-restricted
370 JAK2V617F predominantly induced ECM remodeling in MSC cluster 3 (Supplemental
371 Fig. 7A–C).

372 Thus, our assembloids replicate key features of MPN such as hypoxia,
373 inflammation and fibrotic transformation. Moreover, they confirm and extend previous

374 reports[37,49,50] that basophil progenitors and related cells (e.g., mast cells) may play an
375 important role in MPN pathogenesis.
376
377 **IFNα inhibits EndMT progression in JAK2V617F 3D Assembloids**
378 To assess IFNα's impact on neoplastic vasculature and niche remodeling,
379 JAK2V617F+ assembloids were treated with IFNα for 48h prior to scRNA-seq (Fig.
380 3A). Consistent with our previous findings, IFNα reversed the hyperproliferative
381 phenotype of mutant iEC (Fig. 4A), downregulated EndMT-associated markers
382 (*ACTA2*, *COL1A1*, *Vimentin*) (Fig. 4B) and reduced endothelial outgoing signaling via
383 laminin and VEGF (Fig. 5A).
384 While IFNα reduced interaction strength across the niche (Fig. 5B), basophil
385 progenitors remained a central signaling hub alongside EC, stromal cells, and
386 pericytes, exhibiting increased signaling via ECM components (collagen, FN1) and
387 growth factors (CXCL, VEGF), but decreased TGFβ-mediated output (Fig. 5C). IFNα
388 also reduced megakaryocyte-derived outgoing TGFβ and PDGF signaling.
389 Additionally, IFNα diminished incoming ECM-related signals (collagen, FN1) to stromal
390 cells and pericytes (Fig. 5C). These changes in outgoing and incoming signaling were
391 accompanied by robust activation of JAK–STAT signaling across hematopoietic
392 lineages. In contrast, $CD45^{-}$ populations exhibited limited responsiveness, with
393 pathway activation largely restricted to MSC clusters 1 and 5 and EC. Reactome
394 pathway analysis confirmed a heterogeneous induction of IFNα target genes across
395 hematopoietic and stromal subsets. However, IFNα consistently attenuated the pro-
396 inflammatory transcriptional signature of JAK2V617F+ assembloids, suppressing
397 hypoxia-related pathways in myeloid and stromal compartments (Fig. 5D).
398 These findings highlight IFNα's potential to reverse JAK2V617F-driven
399 endothelial dysfunction and underscore its cell type–specific effects, opening

research avenues for mitigating IFNα-associated side effects such as myalgias and fatigue.

IFNα Inhibits EndMT in Murine Models of PV and MF and in MPN Patients

To validate our findings and assess the translational relevance of our assembloids, we evaluated *in vivo* the effects of IFNα on the BM vasculature using a transgenic JAK2V617F-driven PV mouse model. Eight weeks post-transplantation of JAK2V617F-induced BM cells, pegylated IFNα (pIFNα) or vehicle was administered for 4 or 8 weeks, followed by scRNA-seq analysis of $CD31^{+}CD45^{-}Ter119^{-}$ BM-derived EC (Fig. 6A; Supplemental Fig. 8A). Vehicle-treated mice developed hallmark PV features, including splenomegaly and elevated white blood cells (WBC), red blood cells, hemoglobin, and neutrophil counts (Fig. 6B–C; Supplemental Fig. 8B), but no increase in BM reticulin deposition, consistent with a PV phenotype (Supplemental Fig. 8C). pIFNα treatment reduced WBC and neutrophil counts and increased $Lin^{-}Sca1^{+}$ BM stem and progenitor cells (HSPC), reflecting its known effect on HSPC cycling (Fig. 6C; Supplemental Fig. 8B)[51,52].

scRNA-seq analysis of $CD31^{+}CD45^{-}Ter119^{-}$ BM EC identified four endothelial clusters based on canonical marker expression: arterial, arteriolar, sinusoidal, and blood–brain barrier (BBB)/central nervous system (CNS)-like EC (Fig. 6D; Supplemental Fig. 8D–E; Supplemental Table 12). Consistent with their venous identity, sinusoidal EC showed enrichment of the transcription factor *Nr2f2*[53] and co-expression of the sinusoidal markers *Plvap* and *Stab2*[54,55].

In diseased mice, GSEA revealed progressive upregulation of pathways linked to vascular remodeling (*angiogenesis*, *apical junction*, *coagulation*, *complement*), inflammation (*hypoxia*, *IL6–JAK–STAT3*, *TNFα–NFκB signaling*, *inflammatory response*), and mesenchymal transition (*epithelial–mesenchymal transition*, *TGF-β*

426 *signaling*) in arterial EC from weeks 12 to 16, with a similar, albeit attenuated pattern
427 in arteriolar EC. Correspondingly, genes linked to vascular remodeling (*MMP14*,
428 *TIMP1*), ECM production (*Col1a1*, *Col3a1*, *FN1*), EndMT regulation (*Snai1*, *S100a4*),
429 and mesenchymal identity (*FAP*, *PDGFRA*) were progressively upregulated, consistent
430 with an early EndMT phenotype and aligning with our previous *in vitro* findings
431 (Fig. 4B). pIFNα treatment reversed these pathological signatures and downregulated
432 fibrosis-associated ECM genes like *Col1a1*, while inducing robust IFNα/γ responses
433 across all endothelial subsets (Fig. 6E-F; Supplemental Fig. 9A). This transcriptional
434 modulation was supported by immunofluorescence at 12 weeks, showing increased
435 vascular FSP1 deposition in vehicle-treated mice, which was abrogated by pIFNα
436 treatment (Fig. 6G). Consistent with our transcriptomic and TEM findings in
437 JAK2V617F^{HOM} iEC, EC from diseased mice also showed downregulation of ribosome-
438 and translation-related genes (Fig. 6H; Supplemental Fig. 9B). Concomitant
439 suppression of ribosomal genes, E2F targets, and G2/M checkpoint regulators
440 suggests activation of the integrated stress response (ISR)[56]. ISR activation has been
441 implicated in hypoxia tolerance and endothelial dysfunction, both relevant to fibrotic
442 and cardiovascular diseases[57], but not yet in MPN. These transcriptional
443 dysregulations were reversed after eight weeks of pIFNα treatment (Fig. 6H); however,
444 sinusoidal EC exhibited a comparatively attenuated transcriptional response relative to
445 the arterial and other endothelial subclusters (Supplemental Fig. 9B).

446 To assess pIFNα's anti-EndMT effects in the context of BM fibrosis, we
447 employed a TPO-overexpression murine model recapitulating key features of MF. Four
448 weeks after transplantation of TPO-overexpressing KIT^{+} hematopoietic progenitors,
449 mice received pIFNα or vehicle for an additional four weeks (Fig. 7A). Vehicle-treated
450 mice developed characteristic MF features, including splenomegaly, elevated WBC,
451 and increased BM fibrosis (Fig. 7B–C; Supplemental Fig. 10A). pIFNα treatment

452 reduced spleen size and platelet counts and as shown above, increased $Lin^{-}Sca1^{+}$ BM
453 HSPC, particularly in empty vector controls (Fig. 7B–D).
454 scRNA-seq analysis of $CD31^{+}CD45^{-}Ter119^{-}$ EC identified the same four EC
455 clusters as in the PV model, with the arterial compartment further subdividing into four
456 transcriptionally distinct subclusters: (1) vascular remodeling, (2) vessel sprouting, (3)
457 Snai2+Twist2+ (inflammation/stress signature) and (4) low-cycling progenitor (Fig. 7E,
458 Supplemental Fig. 10B–C). Consistent with the transcriptional changes observed in the
459 PV model from weeks 12 to 16, GSEA revealed inflammatory activation in arterial and
460 arteriolar EC, including upregulation of TNFα, IL-6–JAK–STAT3, and interferon
461 signaling pathways (Fig. 7F). Interestingly, in both the MF murine model and during
462 disease progression in the PV model, arterial and arteriolar EC showed enrichment of
463 IFNα/γ response–associated genes under basal conditions. While this signature was
464 further amplified by pIFNα treatment in the PV model (Fig. 6E), it was suppressed in
465 the MF model (Fig. 7F). EndMT-associated signatures, including upregulation of ECM-
466 related genes, were observed in arterial (especially subclusters 1 and 4) and arteriolar
467 EC, and were downregulated upon pIFNα treatment (Fig. 7G–H, Supplemental
468 Fig. 10D). Immunofluorescence confirmed reduced FSP1 deposition in BM vessels
469 following pIFNα therapy (Fig. 7I). Analysis of BM biopsies from clinically pIFNα-treated
470 MPN patients confirmed IFNα's anti-EndMT effect *in vivo* (Fig. 7J).
471 Together, our findings identify neoplastic arterial remodeling and EndMT as *in*
472 *vivo* hallmarks of MPN, both reversible by IFNα treatment.
473
474
475
476
477

478 **Discussion**

479 Using patient-specific iPSC, we replicated JAK2V617F-driven neoplastic
480 angiogenesis *in vitro*, a hallmark of BM and spleen remodeling in MPN[2,3]. Drug
481 screening with compounds currently used or under investigation for MPN, revealed
482 toxicity profiles consistent with clinical observations, including vascular side effects of
483 anagrelide[58] and venetoclax[59], while ruxolitinib, AMG-232, hydroxyurea, and IFNα
484 demonstrated favorable profiles. pIFNα treatment, approved for PV treatment, has
485 been suggested to improve MF-free survival and preserve near-normal life expectancy
486 in PV[12,60]. However, its mechanisms of action within the malignant clone
487 microenvironment have remained unclear.

488 RNA-seq revealed zygosity-dependent transcriptional programs in iEC at
489 baseline and following IFNα treatment. JAK2V617F^{HOM} iEC showed suppression of
490 translational pathways and disrupted ribosome-ER organization, while JAK2V617F^{HET}
491 iEC exhibited a pro-mesenchymal phenotype consistent with EndMT, a process
492 implicated in the pathogenesis of MF[4]. EndMT has also been linked to endothelial
493 dysfunction in MPN-associated CVD[6], a finding particularly relevant in the context of
494 clonal hematopoiesis of indeterminate potential, where JAK2V617F is among the most
495 common mutations and has been directly implicated in vascular pathology[61]. Zygosity-
496 specific alterations in iEC are consistent with previous findings in erythroid cells, where
497 JAK2V617F^{HOM}, compared to JAK2V617F^{HET}, was associated with enhanced AKT and
498 ERK1/2 signaling[62]. In JAK2V617F^{HET} iEC, dysregulated AKT and ERK1/2 signaling
499 likely promotes EndMT, whereas in JAK2V617F^{HOM} iEC, AKT-driven ROS
500 accumulation[63] may impair ribosome biogenesis[64] and trigger heightened ISR,
501 resulting in translational repression[56]. Although hyperproliferation may contribute to
502 ribosomal disorganization in JAK2V617F^{HOM} iEC, IFNα treatment restored translational

503 programs without inducing apoptosis, consistent with its favorable vascular toxicity
504 profile.

505 In BM niche–mimicking assembloids, we investigated the effects of vascular-
506 restricted JAK2V617F^{HET} expression. Our iPSC-based assembloids supported iEC-
507 MSC pro-angiogenic interactions and recapitulated *in vivo* findings, with acute IFNα
508 exposure enhancing vascularity[65], and chronic exposure suppressing
509 angiogenesis[14,66]. JAK2V617F^{HET} iEC exhibited EndMT, which was reversed by
510 ruxolitinib, nintedanib, and, to a lesser extent, IFNα. scRNA-seq of genotype-controlled
511 assembloids revealed transcriptional homology to native BM, including stromal
512 heterogeneity and hematopoietic–stromal crosstalk[44]. Vascular JAK2V617F^{HET}
513 expression reduced interaction strength between EC and other niche components,
514 consistent with a vascular environment permissive to JAK2V617F clonal expansion[5].

515 Although the mutational burden of the vascular niche *in vivo* remains unclear,
516 recent spatial transcriptomic profiling of BM samples has highlighted vascular niche
517 heterogeneity and revealed activation of pro-inflammatory pathways in MPN patients
518 compared to healthy donors[67]. Our JAK2V617F+ assembloids recapitulated hallmark
519 MPN features, including upregulation of hypoxia-associated genes and TGFβ
520 signaling. The stromal compartment, including pericytes and EC, emerged as a major
521 signaling hub. Consistent with recent findings[50], basophil progenitors also appeared as
522 central mediators of niche-derived signaling, highlighting their potential as therapeutic
523 targets in MPN. Furthermore, the elevated basal IFNα signaling observed in myeloid
524 subsets is consistent with reports of JAK1/STAT1-driven IFNα sensitization in
525 JAK2V617F+ patients[68].

526 Aligning with our *in vitro* findings, in both JAK2V617F-driven PV and TPO-
527 induced MF murine models, EC exhibited pronounced inflammatory signatures (e.g.,
528 TNFα signaling via NF-κB), along robust EndMT. This signature intensified between

529 12- and 16-weeks post-transplantation in the PV model, indicating progressive
530 endothelial dysfunction with disease duration. Concurrently, EC displayed suppression
531 of translation-associated genes, mirroring the transcriptional profile of JAK2V617F^{HOM}
532 iEC *in vitro*.

533 In the MF model and at advanced disease stages in the PV model, EC showed
534 elevated basal IFNα/γ signaling, suggesting a tonic autocrine IFNα loop in EC[14],
535 potentially amplified by inflammatory cues during disease progression. This sustained
536 activation may trigger negative feedback mechanisms that reduce treatment
537 response[69]. Consistently, IFNα-responsive genes were upregulated in the PV model
538 following pIFNα treatment, but downregulated in MF, aligning with the reduced clinical
539 efficacy of IFNα in advanced vs. early-stage MPN[70]. Interestingly, this effect was
540 restricted to arterial and arteriolar EC. Sinusoidal EC displayed increased baseline
541 IFNα/γ signaling only in MF and showed a strong transcriptional response to pIFNα,
542 underscoring subtype-specific dynamics within the BM vascular niche. Such
543 heterogeneity may hold therapeutic relevance, particularly in preventing thrombotic
544 complications and JAK2V617F-driven CVD in MPN. The more pronounced
545 transcriptional dysregulation in arterial and arteriolar EC may partly reflect the scRNA-
546 seq enrichment strategy, which favored CD31^{+}CD45^{-}Ter119^{-} populations and may
547 underrepresent CD31^{low} BM sinusoidal EC[71].

548 Across models, IFNα consistently attenuated inflammatory signaling and
549 EndMT-associated transcriptional programs, along with reduced expression of ECM-
550 related genes. The stronger anti-EndMT and anti-fibrotic effects *in vivo* likely reflect
551 prolonged treatment compared to shorter *in vitro* exposure. This aligns with clinical
552 observations identifying IFNα as a rather slow-acting therapeutic[72]. IFNα anti-EndMT
553 potential was also confirmed in patient BM samples, supporting the translational
554 relevance of our findings.

555 Our findings support a model in which endothelial dysfunction and therapeutic
556 responsiveness of the vascular niche in MPN are shaped by both EC-intrinsic
557 programs and extrinsic inflammatory or clonal cues. Notably, EndMT in JAK2V617F^{HET}
558 iEC was amplified by mutant iHC, while IFNα suppressed EndMT even in assembloids
559 lacking iHC, underscoring endothelial-intrinsic response. These results identify IFNα
560 as a niche-modulating agent capable of cell type-specific transcriptional
561 reprogramming, independent of hematopoietic influence.

562 While our assembloids offer a valuable platform for dissecting vascular niche
563 dynamics, they do not fully recapitulate BM complexity. Future refinements will improve
564 their translational relevance. Using this model alongside established MPN murine
565 systems, we identify neoplastic arterial remodeling and EndMT as hallmarks of MPN.
566 We further demonstrate that IFNα inhibits EndMT, revealing an unrecognized
567 antifibrotic mechanism that may contribute to its long-term disease-modifying effects
568 and hold therapeutic potential in JAK2V617F-driven CVD. Recent evidence of *in utero*
569 JAK2V617F acquisition[73,74], suggests that the mutation might occur at the
570 hemangioblast level. In this context, our findings raise the possibility that mutant EC
571 contribute to early niche dysregulation, promoting malignant clonal expansion. Further
572 single-cell and spatial transcriptomic studies are needed to elucidate the vascular
573 mutational burden in MPN patients and to advance the clinical translation of our
574 findings.

575

576

577

578

579

580

Acknowledgements

This study was supported by the Confocal Microscopy Facility (CMF), the Flow Cytometry Facility (FCF), the Genomics Facility (GF), the Two Photon Imaging Facility (2PIF), and the Immunohistochemistry Facility (IHF), all Core Facilities of the Interdisciplinary Center for Clinical Research (IZKF) Aachen within the Faculty of Medicine at RWTH Aachen University. Transmission Electron Microscopy was performed in the Institute of Pathology and Electron Microscopy Facility, RWTH Aachen. Finally, we would like to thank all the patients who kindly donated samples.

This study was in part funded by grants to Marcelo A. S. de Toledo from the RWTH Aachen University START grant (128/22), to Steffen Koschmieder from the German Research Foundation (Deutsche Forschungsgemeinschaft, DFG) (KO 2155/6-1, project number AOBJ 636363; and KO2155/8-2, project number AOBJ: 680695) and by funds from German Research Foundation as part of the Clinical Research Unit CRU 344 to SK, NC, IC, and THB (KO2155/7-1, CH1509/1-1, GE2811/4-1 and BR1782/5-1). Madeline J. Caduc was funded by the Clinician Scientist Program Junior, the “FF-Med” funding program for female doctors in the post-doc phase of the Faculty of Medicine, RWTH Aachen, Germany and the Mildred-Scheel-Postdoc Program of the German Cancer Aid (Deutsche Krebshilfe, DKH).

Author Contributions

M. J. C.: conceptualization, formal analysis, investigation, visualization, methodology, manuscript–original draft, writing–review and editing. **M. H. E. M.:** methodology. **M. G.:** methodology. **P. W.:** methodology. **K.G.:** methodology. **J. E. P.:** methodology. **D. W. L. W.:** methodology, visualization. **C. B. L.:** methodology. **L. B.:** methodology. **P. S.:** methodology. **B. J.:** methodology. **E. M. B.:** methodology, visualization. **S. E.:** methodology, visualization. **G. M-N.:** resources, investigation, writing-review, and editing. **M. V.:** methodology, visualization. **J. E.:** resources. **P. B.:** resources,

investigation, methodology. **M. A.:** resources, investigation, methodology. **N. C.:** resources, writing-review, and editing. **J. F.:** methodology, writing-review, and editing. **I. G. C.:** resources, methodology. **M. Z.:** resources, investigation, writing-review, and editing. **R. K. S.:** resources, writing-review, and editing**. R. S.:** resources, writing-review, and editing**. T. H. B.:** resources, funding acquisition, writing-review, and editing. **S. K.:** conceptualization, supervision, resources, funding acquisition, project administration, investigation, data analysis, writing-review, and editing. **M. A. S. T.:** conceptualization, supervision, resources, funding acquisition, project administration, investigation, methodology, formal analysis, writing-review, and editing.

Conflict-of-interest disclosure

S. K. received research grant/funding from Geron, Janssen, AOP Pharma, and Novartis; received consulting fees from Pfizer, Incyte, Ariad, Novartis, AOP Pharma, Bristol Myers Squibb, Celgene, Geron, Janssen, CTI BioPharma, Roche, Bayer, GSK, Protagonist, MSD, mPN Hub, Bedrock, and PharmaEssentia; received payment or honoraria from Novartis,BMS/Celgene, Pfizer, Incyte, AOP Orphan, GSK, AbbVie, MSD, MPN Hub, Bedrock, iOMEDICO, and Astra Zeneca; received travel/accommodation support from Alexion, Novartis, Bristol Myers Squibb, Incyte, AOP Pharma, CTI BioPharma, Pfizer, Celgene, Janssen, Geron, Roche, AbbVie, GSK, Sierra Oncology, Kartos, Imago Biosciences, MSD, and iOMEDICO; had a patent issued for a BET inhibitor at RWTH Aachen University; participated on advisory boards for Pfizer, Incyte, Ariad, Novartis, AOP Pharma, BMS, Celgene, Geron, Janssen, CTI BioPharma, Roche, Bayer, GSK, Sierra Oncology, AbbVie, Protagonist, MSD, and PharmaEssentia. **T. H. B.** served as consultant/speaker for Gilead, Janssen, Merck, Novartis, Pfizer, and received research support from Novartis and Pfizer.

References

1. Vannucchi, A. M. *et al.* Mutations and prognosis in primary myelofibrosis. *Leukemia* **27**, 1861–1869 (2013).
2. Boveri, E. *et al.* Bone marrow microvessel density in chronic myeloproliferative disorders: a study of 115 patients with clinicopathological and molecular correlations. *British Journal of Haematology* **140**, 162–168 (2008).
3. Barosi, G. *et al.* Spleen neoangiogenesis in patients with myelofibrosis with myeloid metaplasia. *British Journal of Haematology* **124**, 618–625 (2004).
4. Erba, B. G. *et al.* Endothelial-to-Mesenchymal Transition in Bone Marrow and Spleen of Primary Myelofibrosis. *The American Journal of Pathology* **187**, 1879–1892 (2017).
5. Zhan, H., Lin, C. H. S., Segal, Y. & Kaushansky, K. The JAK2V617F-bearing vascular niche promotes clonal expansion in myeloproliferative neoplasms. *Leukemia* **32**, 462–469 (2018).
6. Zhang, H. *et al.* Decoding Endothelial MPL and JAK2V617F Mutation: Insight Into Cardiovascular Dysfunction in Myeloproliferative Neoplasms. *Arterioscler Thromb Vasc Biol* **44**, 1960–1974 (2024).
7. Sozer, S. *et al.* The presence of JAK2V617F mutation in the liver endothelial cells of patients with Budd-Chiari syndrome. *Blood* **113**, 5246–5249 (2009).
8. Rosti, V. *et al.* Spleen endothelial cells from patients with myelofibrosis harbor the JAK2V617F mutation. *Blood* **121**, 360–368 (2013).
9. Dzierzak, E. & Bigas, A. Blood Development: Hematopoietic Stem Cell Dependence and Independence. *Cell Stem Cell* **22**, 639–651 (2018).
10. Eilken, H. M., Nishikawa, S.-I. & Schroeder, T. Continuous single-cell imaging of blood generation from haemogenic endothelium. *Nature* **457**, 896–900 (2009).
11. Bewersdorf, J. P. *et al.* Moving toward disease modification in polycythemia vera. *Blood* **142**, 1859–1870 (2023).
12. Abu-Zeinah, G. *et al.* Interferon-alpha for treating polycythemia vera yields improved myelofibrosis-free and overall survival. *Leukemia* **35**, 2592–2601 (2021).
13. Indraccolo, S. Interferon-α as angiogenesis inhibitor: Learning from tumor models. *Autoimmunity* **43**, 244–247 (2010).
14. Ciccarese, F. *et al.* Genetic perturbation of IFN-α transcriptional modulators in human endothelial cells uncovers pivotal regulators of angiogenesis. *Comput Struct Biotechnol J* **18**, 3977–3986 (2020).
15. Khan, A. O. *et al.* Human Bone Marrow Organoids for Disease Modeling, Discovery, and Validation of Therapeutic Targets in Hematologic Malignancies. *Cancer Discovery* **13**, 364 (2023).
16. Frenz-Wiessner, S. *et al.* Generation of complex bone marrow organoids from human induced pluripotent stem cells. *Nat Methods* (2024) doi:10.1038/s41592-024-02172-2.
17. Flosdorf, N. *et al.* Proinflammatory phenotype of iPS cell-derived JAK2 V617F megakaryocytes induces fibrosis in 3D in vitro bone marrow niche. *Stem Cell Reports* **19**, 224–238 (2024).
18. Olschok, K. *et al. Stem Cell Reports* **16**, 2768–2783 (2021).
19. Liu, Y. *et al.* Efficient Generation of Megakaryocytes From Human Induced Pluripotent Stem Cells Using Food and Drug Administration-Approved Pharmacological Reagents. *Stem Cells Translational Medicine* **4**, 309–319 (2015).
20. Patsch, C. *et al.* Generation of vascular endothelial and smooth muscle cells from human pluripotent stem cells. *Nat Cell Biol* **17**, 994–1003 (2015).
21. Toledo, M. A. S. *et al.* Nintedanib targets KIT D816V neoplastic cells derived from induced pluripotent stem cells of systemic mastocytosis. *Blood* **137**, 2070–2084 (2021).

686 22. Strassburg, S. *et al.* In vivo evaluation of an electrospun gelatin nonwoven mat for
687 regeneration of epithelial tissues. *J Biomed Mater Res A* **107**, 1605–1614 (2019).
688 23. Caduc, M. J., de Toledo, M. A. S., Koschmieder, S. & Méndez-Ferrer, S. Stem Cell Niche:
689 iPSC-Based Assembloids for Modeling Human Hematopoiesis. *Methods Mol Biol* (2025)
690 doi:10.1007/7651_2025_629.
691 24. Tiedt, R. *et al.* Ratio of mutant JAK2-V617F to wild-type Jak2 determines the MPD
692 phenotypes in transgenic mice. *Blood* **111**, 3931–3940 (2008).
693 25. Schneider, R. K. *et al.* Gli1+ Mesenchymal Stromal Cells Are a Key Driver of Bone
694 Marrow Fibrosis and an Important Cellular Therapeutic Target. *Cell Stem Cell* **20**, 785-800.e8
695 (2017).
696 26. Schubert, M. *et al.* Perturbation-response genes reveal signaling footprints in cancer
697 gene expression. *Nat Commun* **9**, 20 (2018).
698 27. Han, C. *et al.* Chromatin-associated orphan snoRNA regulates DNA damage-mediated
699 differentiation via a non-canonical complex. *Cell Rep* **38**, 110421 (2022).
700 28. Wang, S. *et al.* RNU12 inhibits gastric cancer progression via sponging miR-575 and
701 targeting BLID. *Sci Rep* **13**, 7523 (2023).
702 29. Liu, Z. *et al.* SNORA23 inhibits HCC tumorigenesis by impairing the 2′-O-ribose
703 methylation level of 28S rRNA. *Cancer Biol Med* **19**, 104–119 (2022).
704 30. Bjørn, M. E. & Hasselbalch, H. C. The Role of Reactive Oxygen Species in Myelofibrosis
705 and Related Neoplasms. *Mediators Inflamm* **2015**, 648090 (2015).
706 31. Baumeister, J. *et al.* Hypoxia-inducible factor 1 (HIF-1) is a new therapeutic target in
707 JAK2V617F-positive myeloproliferative neoplasms. *Leukemia* **34**, 1062–1074 (2020).
708 32. Piera-Velazquez, S. & Jimenez, S. A. Endothelial to Mesenchymal Transition: Role in
709 Physiology and in the Pathogenesis of Human Diseases. *Physiol Rev* **99**, 1281–1324 (2019).
710 33. Kvasnicka, H. M. *et al.* Long-term effects of ruxolitinib versus best available therapy on
711 bone marrow fibrosis in patients with myelofibrosis. *J Hematol Oncol* **11**, 42 (2018).
712 34. Bai, Y. *et al.* Ruxolitinib Alleviates Renal Interstitial Fibrosis in UUO Mice. *International*
713 *Journal of Biological Sciences* **16**, 194–203 (2020).
714 35. Yu, W.-K. *et al.* Nintedanib Inhibits Endothelial Mesenchymal Transition in Bleomycin-
715 Induced Pulmonary Fibrosis via Focal Adhesion Kinase Activity Reduction. *Int J Mol Sci* **23**,
716 8193 (2022).
717 36. Vachhani, P. *et al.* Interferons in the treatment of myeloproliferative neoplasms. *Ther*
718 *Adv Hematol* **15**, 20406207241229588 (2024).
719 37. Toledo, M. A. S., Chatain, N., Zenke, M. & Koschmieder, S. Mast cells as a therapeutic
720 target in myeloproliferative neoplasms. *Trends in Molecular Medicine* **28**, 902–905 (2022).
721 38. Sweeney, M. & Foldes, G. It Takes Two: Endothelial-Perivascular Cell Cross-Talk in
722 Vascular Development and Disease. *Frontiers in Cardiovascular Medicine* **5**, (2018).
723 39. Slenders, L. *et al.* Identification of endothelial-to-mesenchymal transition gene
724 signatures in single-cell transcriptomics of human atherosclerotic tissue. 2023.07.18.549599
725 Preprint at https://doi.org/10.1101/2023.07.18.549599 (2023).
726 40. Xie, W. *et al.* Multi-Transcriptomic Analysis Reveals the Heterogeneity and Tumor-
727 Promoting Role of SPP1/CD44-Mediated Intratumoral Crosstalk in Gastric Cancer. *Cancers* **15**,
728 164 (2022).
729 41. Wang, H. *et al.* FN1 is a prognostic biomarker and correlated with immune infiltrates
730 in gastric cancers. *Frontiers in Oncology* **12**, 918719 (2022).
731 42. Pritchard, J. E. *et al.* Non-canonical Hedgehog signaling mediates profibrotic
732 hematopoiesis-stroma crosstalk in myeloproliferative neoplasms. *Cell Rep* **43**, 113608 (2024).

43. Li, R. *et al.* A pro-inflammatory stem cell niche drives myelofibrosis through a targetable galectin 1 axis. 2023.08.05.550630 Preprint at https://doi.org/10.1101/2023.08.05.550630 (2023).
44. Leimkühler, N. B. *et al.* Heterogeneous bone-marrow stromal progenitors drive myelofibrosis via a druggable alarmin axis. *Cell Stem Cell* **28**, 637-652.e8 (2021).
45. Huang, E. *et al.* The Roles of Immune Cells in the Pathogenesis of Fibrosis. *International Journal of Molecular Sciences* **21**, 5203 (2020).
46. Meng, X.-M., Nikolic-Paterson, D. J. & Lan, H. Y. TGF-β: the master regulator of fibrosis. *Nat Rev Nephrol* **12**, 325–338 (2016).
47. Sarkaria, S. M. *et al.* Systematic dissection of coordinated stromal remodeling identifies *Sox10*+ glial cells as a therapeutic target in myelofibrosis. *Cell Stem Cell* **30**, 832-850.e6 (2023).
48. Bahar, M. E., Kim, H. J. & Kim, D. R. Targeting the RAS/RAF/MAPK pathway for cancer therapy: from mechanism to clinical studies. *Sig Transduct Target Ther* **8**, 1–38 (2023).
49. Melo-Cardenas, J. *et al.* IL13 Contributes to Fibrotic Progression of the Myeloproliferative Neoplasms. *Blood* **138**, 60 (2021).
50. Li, R. *et al.* A proinflammatory stem cell niche drives myelofibrosis through a targetable galectin-1 axis. *Sci Transl Med* **16**, eadj7552 (2024).
51. Demerdash, Y., Kain, B., Essers, M. A. G. & King, K. Y. Yin and Yang: The dual effects of interferons on hematopoiesis. *Experimental Hematology* **96**, 1–12 (2021).
52. Essers, M. A. G. *et al.* IFNα activates dormant haematopoietic stem cells in vivo. *Nature* **458**, 904–908 (2009).
53. Sissaoui, S. *et al.* Genomic Characterization of Endothelial Enhancers Reveals a Multifunctional Role for NR2F2 in Regulation of Arteriovenous Gene Expression. *Circulation Research* **126**, 875–888 (2020).
54. Denzer, L., Muranyi, W., Schroten, H. & Schwerk, C. The role of PLVAP in endothelial cells. *Cell Tissue Res* **392**, 393–412 (2023).
55. Iga, T. *et al.* Spatial heterogeneity of bone marrow endothelial cells unveils a distinct subtype in the epiphysis. *Nat Cell Biol* **25**, 1415–1425 (2023).
56. Costa-Mattioli, M. & Walter, P. The integrated stress response: From mechanism to disease. *Science* **368**, eaat5314 (2020).
57. Santos-Ribeiro, D., Godinas, L., Pilette, C. & Perros, F. The integrated stress response system in cardiovascular disease. *Drug Discovery Today* **23**, 920–929 (2018).
58. James, C. W. Anagrelide-induced cardiomyopathy. *Pharmacotherapy* **20**, 1224–1227 (2000).
59. AlAsmari, A. F. *et al.* Venetoclax Induces Cardiotoxicity through Modulation of Oxidative-Stress-Mediated Cardiac Inflammation and Apoptosis via NF-κB and BCL-2 Pathway. *Int J Mol Sci* **23**, 6260 (2022).
60. Abu-Zeinah, G., Silver, R. T., Abu-Zeinah, K. & Scandura, J. M. Normal life expectancy for polycythemia vera (PV) patients is possible. *Leukemia* **36**, 569–572 (2022).
61. Misaka, T., Kimishima, Y., Yokokawa, T., Ikeda, K. & Takeishi, Y. Clonal hematopoiesis and cardiovascular diseases: role of JAK2V617F. *Journal of Cardiology* **81**, 3–9 (2023).
62. Akada, H. *et al.* Conditional expression of heterozygous or homozygous Jak2V617F from its endogenous promoter induces a polycythemia vera-like disease. *Blood* **115**, 3589–3597 (2010).
63. Marty, C. *et al.* A role for reactive oxygen species in JAK2 V617F myeloproliferative neoplasm progression. *Leukemia* **27**, 2187–2195 (2013).

64. Willi, J. *et al.* Oxidative stress damages rRNA inside the ribosome and differentially affects the catalytic center. *Nucleic Acids Research* **46**, 1945–1957 (2018).
65. Prendergast, Á. M. *et al.* IFNα-mediated remodeling of endothelial cells in the bone marrow niche. *Haematologica* **102**, 445–453 (2017).
66. Pammer, J. *et al.* Interferon-a prevents apoptosis of endothelial cells after short-term exposure but induces replicative senescence after continuous stimulation. *Laboratory Investigation* 11 (2006).
67. Castorena, J. *et al.* Spatial Transcriptomic Profiling of Bone Marrow Vascular Niches Unveils an Endothelial Stress Signature in Myeloproliferative Neoplasms. *Blood* **144**, 4516 (2024).
68. Czech, J. *et al.* JAK2V617F but not CALR mutations confer increased molecular responses to interferon-α via JAK1/STAT1 activation. *Leukemia* **33**, 995–1010 (2019).
69. Usart, M. *et al.* Loss of Socs2 improves molecular responses to IFNα in a mouse model of myeloproliferative neoplasms driven by JAK2-V617F. *Leukemia* **39**, 876–887 (2025).
70. Kiladjian, J.-J., Mesa, R. A. & Hoffman, R. The renaissance of interferon therapy for the treatment of myeloid malignancies. *Blood* **117**, 4706–4715 (2011).
71. Kenswil, K. J. G. *et al.* Characterization of Endothelial Cells Associated with Hematopoietic Niche Formation in Humans Identifies IL-33 As an Anabolic Factor. *Cell Reports* **22**, 666–678 (2018).
72. Gisslinger, H. *et al.* Long-Term Efficacy and Safety of Ropeginterferon Alfa-2b in Patients with Polycythemia Vera — Final Phase I/II Peginvera Study Results. *Blood* **132**, 3030 (2018).
73. Sousos, N. *et al.* In utero origin of myelofibrosis presenting in adult monozygotic twins. *Nat Med* **28**, 1207–1211 (2022).
74. Williams, N. *et al.* Driver Mutation Acquisition in Utero and Childhood Followed By Lifelong Clonal Evolution Underlie Myeloproliferative Neoplasms. *Blood* **136**, LBA-1 (2020).

828 **Figure Legends**

829 **Figure 1. MPN Patient-derived iEC display zygosity-specific transcriptional**
830 **responses to IFNα treatment**

831 (A) Heatmap depicting unsupervised clustering of differentially regulated genes in
832 $JAK2^{WT}$ and $JAK2V617F^{HET\ and\ HOM}$ iEC (cut off: absolute logarithmic fold change
833 >1).

834 (B) Volcano plot displaying DEG in iEC following IFNα treatment. A total of 168
835 genes were upregulated, while 10 were downregulated. Abbreviations: NS, non-
836 significant; Log2FC, logarithmic fold change. The accompanying Venn diagram
837 highlights overlapping and significantly enriched genes within each genotype
838 after IFNα treatment (FDR < 0.05). A complete list of all significantly
839 dysregulated genes is provided in Supplemental Table 10.

840 (C) Selection of dysregulated gene sets illustrating the prominent aspects detected
841 in GSEA affecting $JAK2V617F^{HOM}$ iEC biology. Abbreviations: NP, nominal p-
842 value; FDR, false discovery rate.

843 (D) Quantification of mRNA levels of RNA, Ro60-Associated Y3 (*RNY3*) by RT-
844 qPCR in $JAK2V617F^{HOM}$ iEC, relative to $JAK2^{WT}$ iEC. Unpaired t-test (n = 5-6).

845 (E) Representative TEM images of iEC of indicated JAK2V617F zygosity. N marks
846 the nucleus, white arrows depict rough endoplasmic reticulum, and red arrows
847 showcase accumulated loose ribosomes in mutated iEC. Scale bar: 1,000 nm.

848 (F) Quantification of normalized mRNA read counts for RNA, U12 small nuclear
849 (*RNU12*), Small Nucleolar RNA, H/ACA Box 23 (*SNORA23*), *RNY3*, and RNA,
850 U5E small nuclear 1 (*RNU5E-1*) expression in untreated versus IFNα-treated
851 $JAK2V617F^{HOM}$ iEC (n = 3).

852 (G) GO analysis depicting upregulated terms in JAK2V617F^{HOM} iEC following IFNα
853 treatment. The size of the dots reflects the number of dysregulated genes from
854 the gene list associated with the GO term, while the color of the dots represents
855 the adjusted p-value (p. adjust).
856 (H) Selected dysregulated gene sets from GSEA highlighting key pathways altered
857 in JAK2V617F^{HET} iEC. Abbreviations: NP, nominal p-value; FDR, false discovery
858 rate.

859 (I) Quantification of mRNA levels of fibroblast-specific protein 1 (*FSP1*), alpha-
860 smooth muscle actin (*ACTA2*) by RT-qPCR in JAK2V617F^{HET} iEC, relative to
861 JAK2^{WT} iEC. Unpaired t-test (n = 3-8).

862 **Figure 2. Modeling JAK2V617F-driven EndMT in iPSC-based assembloids**

863 (A) Schematic representation of the experimental setup. After vascular tree
864 formation, WT and JAK2V617F^{HET} iEC assembloids were pre-treated with
865 IFNα (1000 U/ml) or with a tyrosine kinase inhibitor (TKI): ruxolitinib (RUX, 250
866 nM), nintedanib (NIN, 250 nM), or a combination of ruxolitinib and nintedanib
867 (both 250 nM). EndMT was then induced using pro-fibrotic cytokines (IL1β,
868 TNFα, and TGFβ) to mimic the pathological conditions of MF. (a)
869 Representative confocal image shows MSC alignment along the walls of tube-
870 like structures, mimicking the physiological EC-pericyte arrangement. iEC
871 (red) and MSC (green) were labeled with fluorescent cell linkers PKH26 and
872 PKH67, respectively. Nuclei are stained with DAPI. Scale bar: 100 µm.
873 (B) Representative IF of JAK2^{WT} and JAK2V617F^{HET} 3D assembloids, stained for
874 CD31 (green) and FSP1 (red) to indicate EndMT. Cell nuclei are visualized
875 using DAPI (blue). Scale bar: 125 µm. Quantification of FSP1 fluorescence area

876 in $JAK2^{WT}$ and $JAK2V617F^{HET}$ assembloids under both stimulated and
877 unstimulated conditions. Two-way ANOVA (n = 3).
878 (C) Representative duplex IF showing FSP1 expression in a $CD31^{+}$ iEC following
879 exposure to IL1β, TNFα, and TGFβ in $JAK2V617F^{HET}$ 3D assembloids. Scale
880 bar: 10 µm. Fold induction quantification of FSP1-CD31 fluorescence
881 colocalization in $JAK2^{WT}$ vs. $JAK2V617F^{HET}$ 3D assembloids after cytokine
882 stimulation. Unpaired t-test (n = 3).
883 (D) Representative IF of $JAK2V617F^{HET}$ assembloids under basal conditions and
884 after pro-fibrotic cytokine exposure, stained for αSMA (green), with DAPI (blue)
885 highlighting cell nuclei. Quantitative analysis of mean fluorescence intensity
886 (MFI) for αSMA was conducted in mutated and unmutated assembloids. Two-
887 way ANOVA (n = 3). Scale bars: 250 µm.
888 (E) Representative immunofluorescence images of assembloids stained for CD31
889 (green), FSP1 (red), and nuclei (DAPI, blue) under different treatment
890 conditions. Scale bar: 125 µm.
891 (F) Quantification of FSP1 fluorescence area in cytokine-treated 3D assembloids
892 following sensitization with IFNα, nintedanib, ruxolitinib, or their combination.
893 Statistical analysis by one-way ANOVA (n = 3).
894 (G) Quantification of FSP1–CD31 colocalization in $JAK2^{WT}$ and $JAK2V617F^{HET}$ 3D
895 assembloids under different treatment conditions, using Mander's colocalization
896 coefficient (M1). One-way ANOVA (n = 3).

897 MFI quantification of pro-fibrotic ECM components (H) Col1a1 and (I) αSMA in
898 3D assembloids pre-treated with IFNα, nintedanib, ruxolitinib, or their
899 combination, followed by cytokine exposure. One-way ANOVA (n = 3).

900

901 **Figure 3. Assembloids mimic key cellular interactions of the human BM niche**

902 (A) Schematic of the experimental setup for the generation of 3D assembloids for
903 scRNAseq. JAK2^{WT} or JAK2V617F^{HET} iPSC-derived megakaryocytes (iMK),
904 monocytes/macrophages (iM), and granulocytes (iGr) (collectively referred to
905 as iPSC-derived hematopoietic cells (iHC)) were mixed in a 2:1:1 ratio and
906 combined with MSC and JAK2^{WT} or JAK2V617F^{HET} iEC within fibrin hydrogels.
907 To evaluate the effect of IFNα on the mutant niche, JAK2V617F^{HET} assembloids
908 were treated with IFNα (1000 U/ml) for 48h before scRNAseq.
909 (B) Uniform Manifold Approximation and Projection (UMAP) plot showing the
910 isolated hematopoietic and stromal clusters. Abbreviations: Mono – monocytes;
911 MSC – mesenchymal stromal cells; Mast – mast cells; Eo – eosinophils; Neu –
912 neutrophils; DC – dendritic cells; EC – endothelial cells; BasoP – basophil
913 progenitors; HemoEndo – hemogenic endothelium; MK – megakaryocytes;
914 HPC – hematopoietic progenitor cells; Peri – pericytes; Astro – astrocytes.
915 (C) Circle plot depicting the mapping of ligand-receptor (L-R) interactions among
916 various cell types in JAK2^{WT} (WT-WT) assembloids. Each node represents a
917 distinct cell type, with MSC clusters categorized as stromal cells. Line thickness
918 indicates interaction strength, while arrows denote the direction of the
919 interactions.
920 (D) Heatmap illustrating the relative strength of incoming and outgoing signaling
921 among various cell types in JAK2^{WT} assembloids. Rows represent aggregate
922 strength of signaling for the given pathway, while columns indicate distinct cell
923 types. The color code reflects the strength of the interactions.

924

925 **Figure 4. JAK2V617F^{HET} assembloids recapitulate key MPN features**

926 (A) Quantification of relative EC numbers in 3D assembloids.

927 (B) Dot plots with error bars showing the normalized expression levels of selected
928 EndMT markers in EC from 3D assembloids.

929 In figure (A) and (B) the color code in the figure represents different genetic
930 backgrounds and treatment conditions: blue for JAK2^{WT} assembloids, yellow for
931 assembloids with vascular-specific JAK2V617F^{HET} expression, orange for
932 JAK2V617F^{HET} assembloids, and green for JAK2V617F^{HET} assembloids treated
933 with IFNα (1000 U/ml) for 48 hours prior to scRNA-seq.

934 (C) Circle plot illustrating the overall ligand-receptor (L-R) interaction strength
935 among various cell types in JAK2V617F^{HET} versus JAK2^{WT} assembloids. Each
936 node represents a distinct cell type, with MSC clusters classified as stromal
937 cells. Line thickness reflects interaction strength, and arrows indicate the
938 direction of interactions. Red lines indicate increased interaction strength, while
939 blue lines denote decreased interaction strength.

940 (D) Heatmap illustrating the relative strength of incoming and outgoing signaling
941 among various cell types in JAK2V617F^{HET} assembloids. Rows represent
942 aggregate strength of signaling for the given pathway, while columns indicate
943 distinct cell types. The color code reflects the strength of the interactions.

944 (E) PROGENy analysis and Area Under the Curve (AUC) score analysis of selected
945 pathways in JAK2V617F^{HET} (HET-HET) compared to JAK2^{WT} assembloids (WT-
946 WT). Abbreviations: FC – Fold change of HET-HET vs. WT-WT assembloids.

947

948 **Figure 5. IFNα mitigates pro-fibrotic signaling in JAK2V617F^{HET} assembloids**

949 (A) Heatmap showing differential incoming and outgoing signaling in iEC based on
950 L-R analysis from scRNA-seq experiment. The columns represent the tested
951 conditions: (1) HET-WT vs. WT-WT, (2) HET-HET vs. WT-WT, and (3) HET-
952 HET + IFNα vs. HET-HET. Each row corresponds to a mediator of interaction.
953 The color gradient from red to blue indicates increasing to decreasing difference
954 in interaction strength mediated by the listed factors.

955 (B) Circle plot illustrating the overall L-R interaction strength among various cell
956 types in IFNα-treated versus untreated JAK2V617F^{HET} assembloids (HET-HET
957 + IFNα vs. HET-HET). Each node represents a distinct cell type, with MSC
958 clusters categorized as stromal cells. Line thickness denotes interaction
959 strength, while arrows indicate interaction direction. Red lines represent
960 increased interaction strength, whereas blue lines indicate decreased
961 interaction strength.

962 (C) Heatmap illustrating the relative strength of incoming and outgoing signaling
963 among various cell types in JAK2V617F^{HET} assembloids treated with IFNα.
964 Rows represent aggregate strength of signaling for the given pathway, while
965 columns indicate distinct cell types. The color code reflects the strength of the
966 interactions.

967 (D) PROGENy analysis and AUC score analysis of selected pathways in
968 JAK2V617F^{HET} assembloids treated with IFNα (HET-HET + IFNα) compared to
969 untreated JAK2V617F^{HET} assembloids (HET-HET). Abbreviations: FC – Fold
970 change of HET-HET + IFNα vs. HET-HET cocultures.

971

972 **Figure 6. IFNα reverses EndMT and restores endothelial transcriptional**
973 **programs in a JAK2V617F-driven PV mouse model**

974 (A) Schematic overview of the experimental workflow using the transgenic
975 JAK2V617F-driven PV mouse model. Eight weeks post BM transplantation,
976 pIFNα was administered for 4 or 8 weeks. $CD31^{+}CD45^{-}Ter119^{-}$ BM-derived EC
977 were isolated for scRNA-seq analysis to assess transcriptional changes in
978 response to treatment.
979 (B) Representative images and quantification of spleen size across groups.
980 (C) Peripheral white blood cells (WBC), neutrophil, red blood cells (RBC), and
981 hemoglobin (HGB) levels, and percentage of $Lin^{-}Sca1^{+}$ cells in BM from treated
982 and untreated WT and JAK2V617F mice 16 weeks post-engraftment. Two-way
983 ANOVA (n = 5–6).
984 (D) UMAP of $CD31^{+}CD45^{-}Ter119^{-}$ BM-derived EC clusters identified by
985 scRNAseq.
986 (E) GSEA heatmap showing hallmark pathway enrichment across endothelial
987 subtypes (arteriolar, arterial, BBB/CNS-like, and sinusoidal EC) from scRNA-
988 seq of BM-derived EC 16 weeks post-engraftment. Comparisons: JAK2V617F
989 vs. WT (–), and JAK2V617F + pIFNα vs. JAK2V617F (+).
990 (F) Dot plot showing expression of selected genes across endothelial clusters from
991 WT and JAK2V617F PV mice treated with or without pIFNα for 4 or 8 weeks.
992 Dot size represents the percentage of cells expressing each gene; color scale
993 indicates average expression level (Z-score). Genes are grouped by functional
994 annotation: endothelial markers (blue), and vascular remodeling/EndMT-
995 associated genes (orange).

996 (G) Representative IF of BM sections stained for FSP1 (red) and CD31 (green) in
997 WT and JAK2V617F mice ± pIFNα treatment. Nuclei are counterstained with
998 DAPI (blue). Arrows denote EC. Scale: 10 μm. Quantitative analysis of global
999 and vessel-specific mean FSP1 fluorescence intensity.
1000 (H) GSEA for pathways related to cytoplasmic translation (C.T.) and ribosome in
1001 endothelial clusters from WT and JAK2V617F mice following 4 weeks (top) and
1002 8 weeks (bottom) of pIFNα treatment. Color scale represents enrichment
1003 scores; asterisks indicate statistical significance.

1004 **Figure 7. IFNα suppresses EndMT signatures in a murine model of MF**

1005 (A) Schematic overview of the experimental workflow in the TPO-overexpression
1006 MF mouse model. Four weeks after KIT^+ BM cell transplantation, pIFNα was
1007 administered for 4 weeks. $CD31^+CD45^-Ter119^-$ BM EC were isolated and
1008 subjected to scRNA-seq to assess treatment-associated transcriptional
1009 changes.
1010 (B) Representative spleen images and quantification of spleen size across groups.
1011 (C) Peripheral white blood cell (WBC) and platelet (PLT) counts,
1012 (D) and percentage of Lin^-Sca1^+ progenitor cells in BM. Two-way ANOVA (n = 5).
1013 (E) UMAP of $CD31^+CD45^-Ter119^-$ BM-derived EC clusters identified by
1014 scRNAseq.
1015 (F) GSEA heatmap displaying pathway enrichment in endothelial clusters.
1016 Comparisons: TPO-OE vs. EV (–), and TPO-OE + pIFNα vs. TPO-OE (+).
1017 (G) GSEA heatmaps displaying enrichment scores for the curated EndMT signature
1018 across endothelial clusters and
1019 (H) arterial EC subclusters.

1020 (I) Representative IF images of BM sections from EV and TPO-OE mice, treated
1021 or not with pIFNα for 4 weeks. Sections were stained for CD31 (green), FSP1
1022 (red), and DAPI (blue). Asterisks denote vessel lumens and arrows indicate EC.
1023 Scale: 10 μm. Quantification of global and vessel-specific mean FSP1
1024 fluorescence intensity. Two-way ANOVA (n = 4-6).
1025 (J) IF images of BM sections from MPN patients treated with pIFNα, stained for
1026 CD31 (green), FSP1 (red), and DAPI (blue). Arrows indicate EC. Scale: 25 μm.
1027 Quantification of global and vessel-specific mean FSP1 fluorescence intensity,
1028 normalized to baseline. One sample t-test (n = 3). Color indicates individual
1029 patients; detailed patient information is provided in the Supplemental
1030 Information.

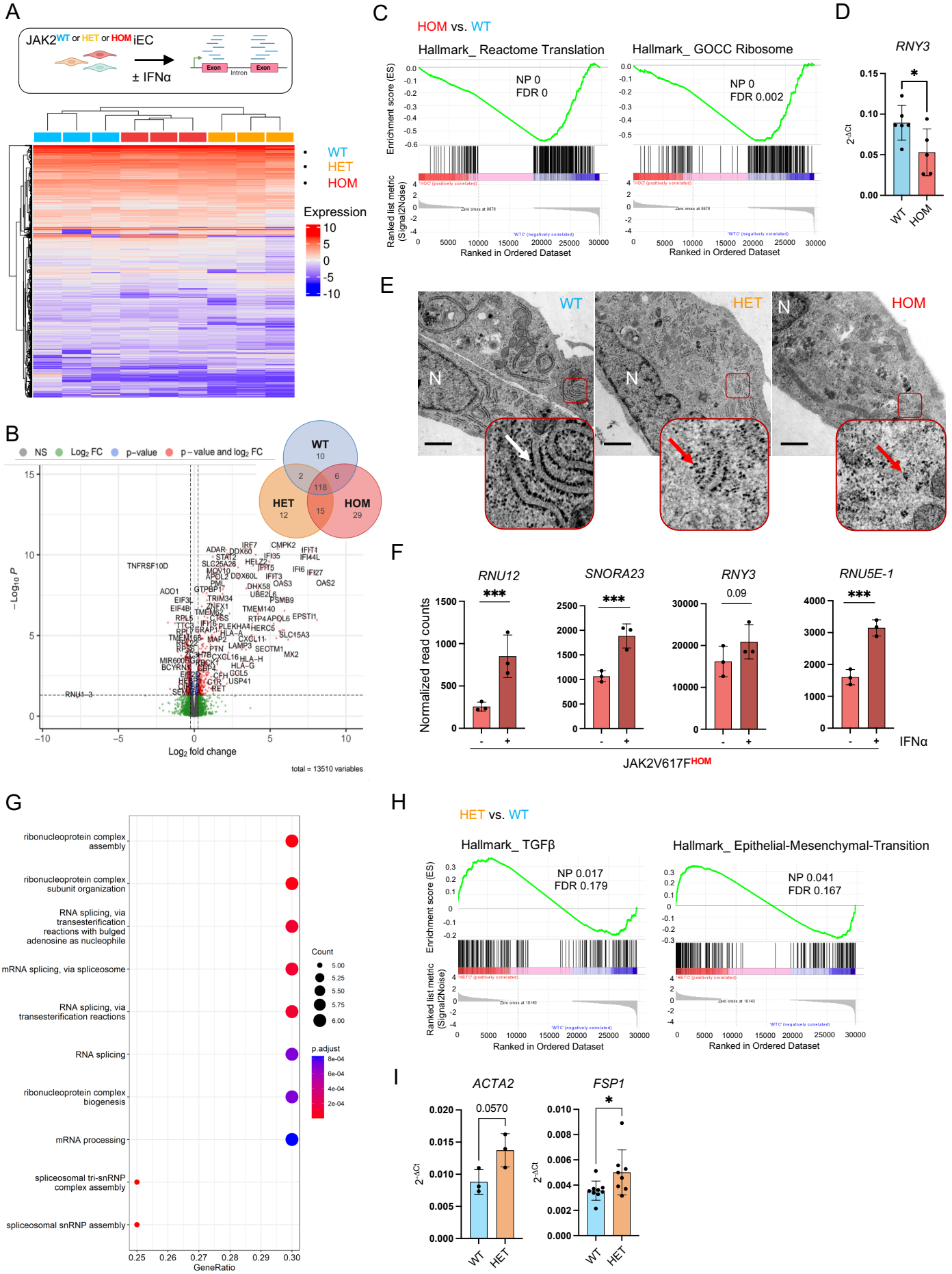
A
JAK2WT or HET or HOM iEC
± IFNα
Exon
Intron
Exon
WT
HET
HOM
Expression
10
5
0
-5
-10
B
NS
Log2 FC
p-value
p-value and log2 FC
WT
10
HET
12
HOM
29
2
6
118
15
TNFRSF10D
RNU1-3
−Log10 P
Log2 fold change
total = 13510 variables
C
HOM vs. WT
Hallmark_ Reactome Translation
NP 0
FDR 0
Hallmark_ GOCC Ribosome
NP 0
FDR 0.002
Enrichment score (ES)
Ranked list metric (Signal2Noise)
Ranked in Ordered Dataset
D
RNY3
2-ΔCt
WT
HOM
E
WT
HET
HOM
N
F
RNU12
SNORA23
RNY3
RNU5E-1
Normalized read counts
0.09
IFNα
JAK2V617FHOM
G
ribonucleoprotein complex assembly
ribonucleoprotein complex subunit organization
RNA splicing, via transesterification reactions with bulged adenosine as nucleophile
mRNA splicing, via spliceosome
RNA splicing, via transesterification reactions
RNA splicing
ribonucleoprotein complex biogenesis
mRNA processing
spliceosomal tri-snRNP complex assembly
spliceosomal snRNP assembly
Count
p.adjust
GeneRatio
H
HET vs. WT
Hallmark_ TGFβ
NP 0.017
FDR 0.179
Hallmark_ Epithelial-Mesenchymal-Transition
NP 0.041
FDR 0.167
Enrichment score (ES)
Ranked list metric (Signal2Noise)
Ranked in Ordered Dataset
I
ACTA2
0.0570
FSP1
2-ΔCt
WT
HET

Fig. 1

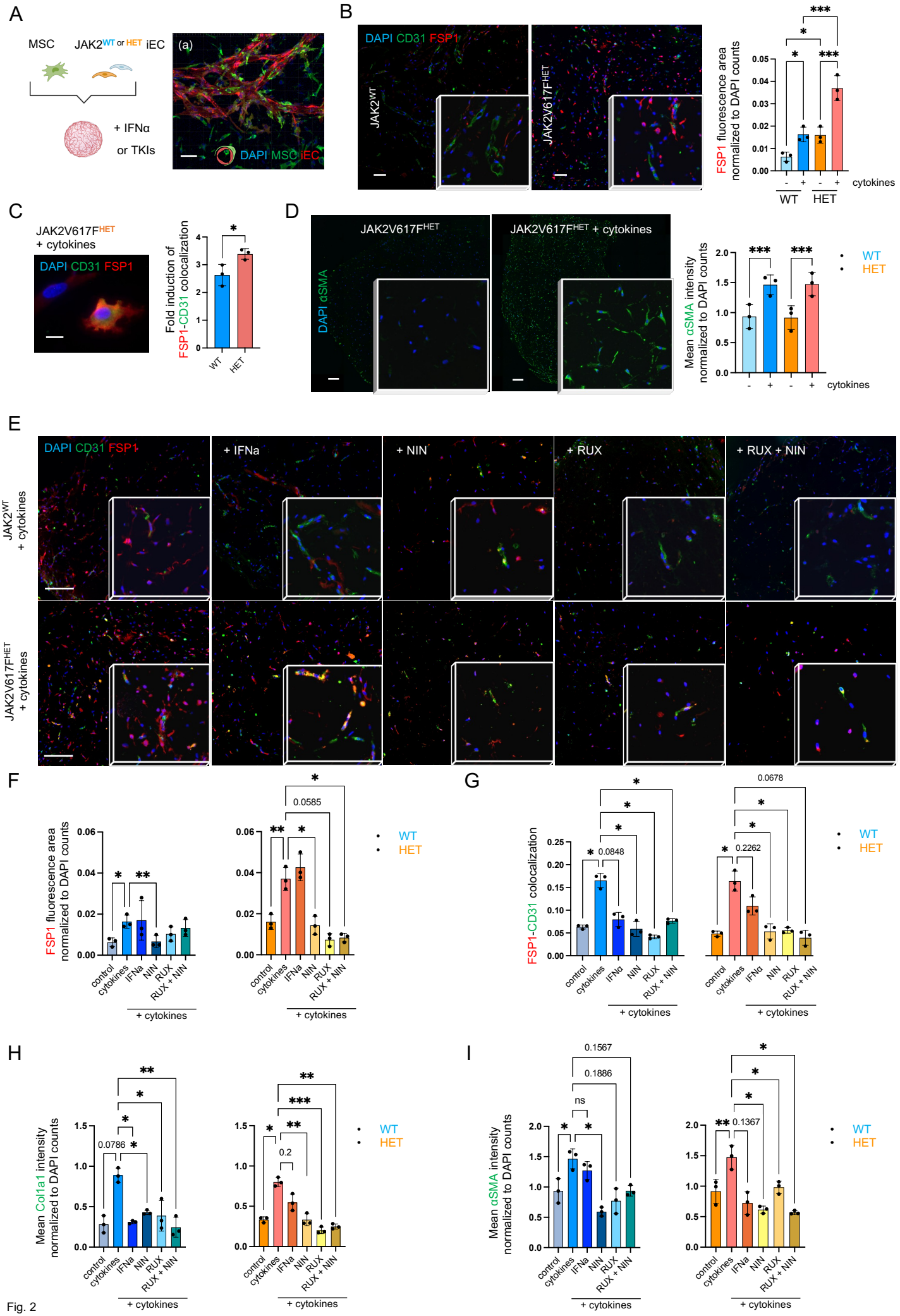
A
MSC
JAK2WT or HET iEC
+ IFNα
or TKIs
(a)
DAPI MSC iEC
B
DAPI CD31 FSP1
JAK2WT
JAK2V617FHET
FSP1 fluorescence area normalized to DAPI counts
cytokines
WT
HET
C
JAK2V617FHET
+ cytokines
DAPI CD31 FSP1
Fold induction of FSP1-CD31 colocalization
D
JAK2V617FHET
JAK2V617FHET + cytokines
DAPI αSMA
Mean αSMA intensity normalized to DAPI counts
E
DAPI CD31 FSP1
+ IFNa
+ NIN
+ RUX
+ RUX + NIN
JAK2WT + cytokines
JAK2V617FHET + cytokines
F
FSP1 fluorescence area normalized to DAPI counts
control
cytokines
IFNa
NIN
RUX
RUX + NIN
+ cytokines
G
FSP1-CD31 colocalization
H
Mean Col1a1 intensity normalized to DAPI counts
I
Mean αSMA intensity normalized to DAPI counts

Fig. 2

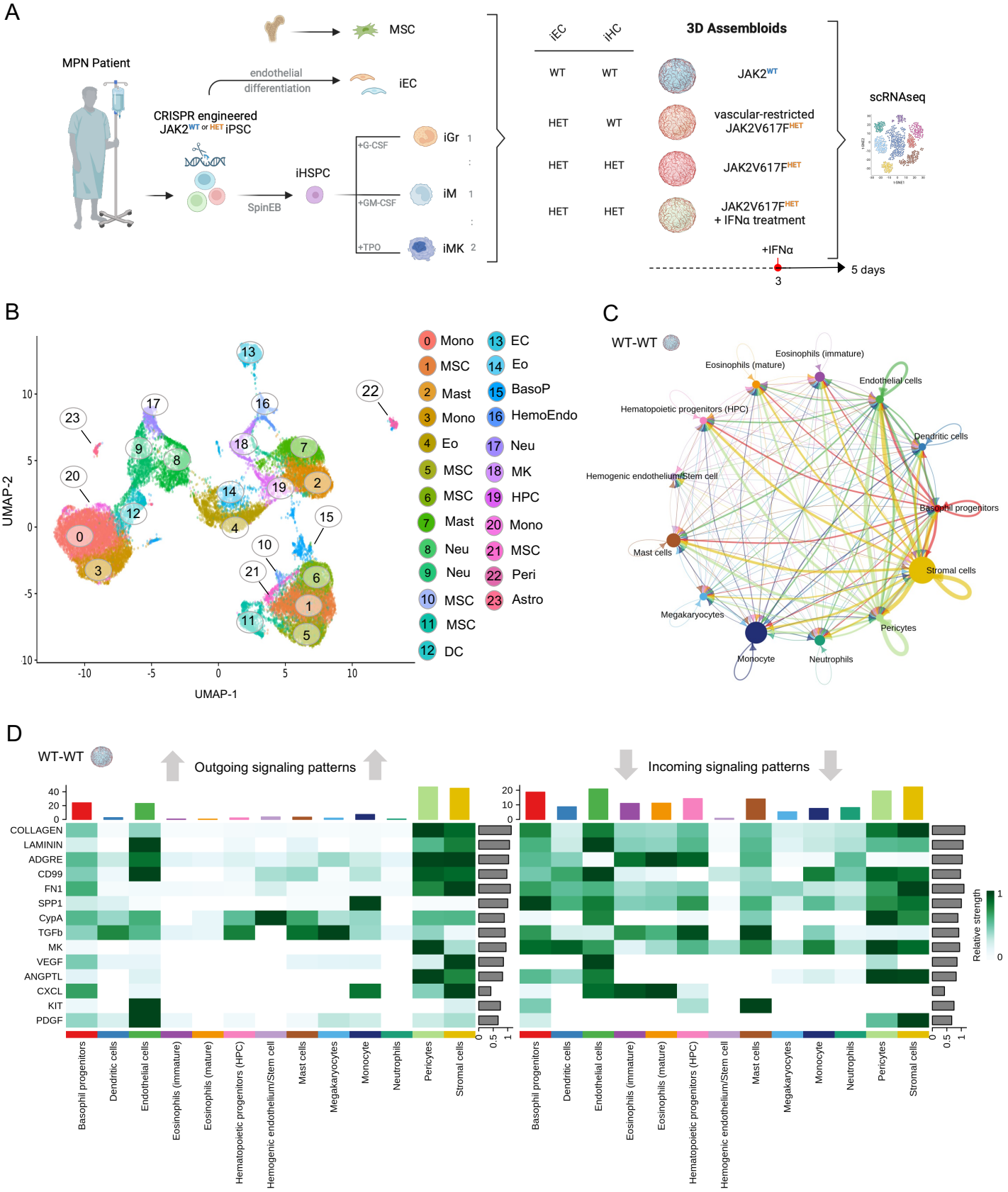
A
MPN Patient
MSC
endothelial differentiation
iEC
CRISPR engineered JAK2WT or HET iPSC
SpinEB
iHSPC
+G-CSF
+GM-CSF
+TPO
iGr 1
iM 1
iMK 2
iEC
iHC
3D Assembloids
WT WT JAK2WT
HET WT vascular-restricted JAK2V617FHET
HET HET JAK2V617FHET
HET HET JAK2V617FHET + IFNα treatment
+IFNα
3
5 days
scRNAseq
B
UMAP-2
UMAP-1
0 Mono
1 MSC
2 Mast
3 Mono
4 Eo
5 MSC
6 MSC
7 Mast
8 Neu
9 Neu
10 MSC
11 MSC
12 DC
13 EC
14 Eo
15 BasoP
16 HemoEndo
17 Neu
18 MK
19 HPC
20 Mono
21 MSC
22 Peri
23 Astro
C
WT-WT
Eosinophils (immature)
Eosinophils (mature)
Endothelial cells
Hematopoietic progenitors (HPC)
Dendritic cells
Hemogenic endothelium/Stem cell
Basophil progenitors
Mast cells
Stromal cells
Megakaryocytes
Pericytes
Monocyte
Neutrophils
D
WT-WT
Outgoing signaling patterns
Incoming signaling patterns
COLLAGEN
LAMININ
ADGRE
CD99
FN1
SPP1
CypA
TGFb
MK
VEGF
ANGPTL
CXCL
KIT
PDGF
Basophil progenitors
Dendritic cells
Endothelial cells
Eosinophils (immature)
Eosinophils (mature)
Hematopoietic progenitors (HPC)
Hemogenic endothelium/Stem cell
Mast cells
Megakaryocytes
Monocyte
Neutrophils
Pericytes
Stromal cells
Relative strength

Fig. 3

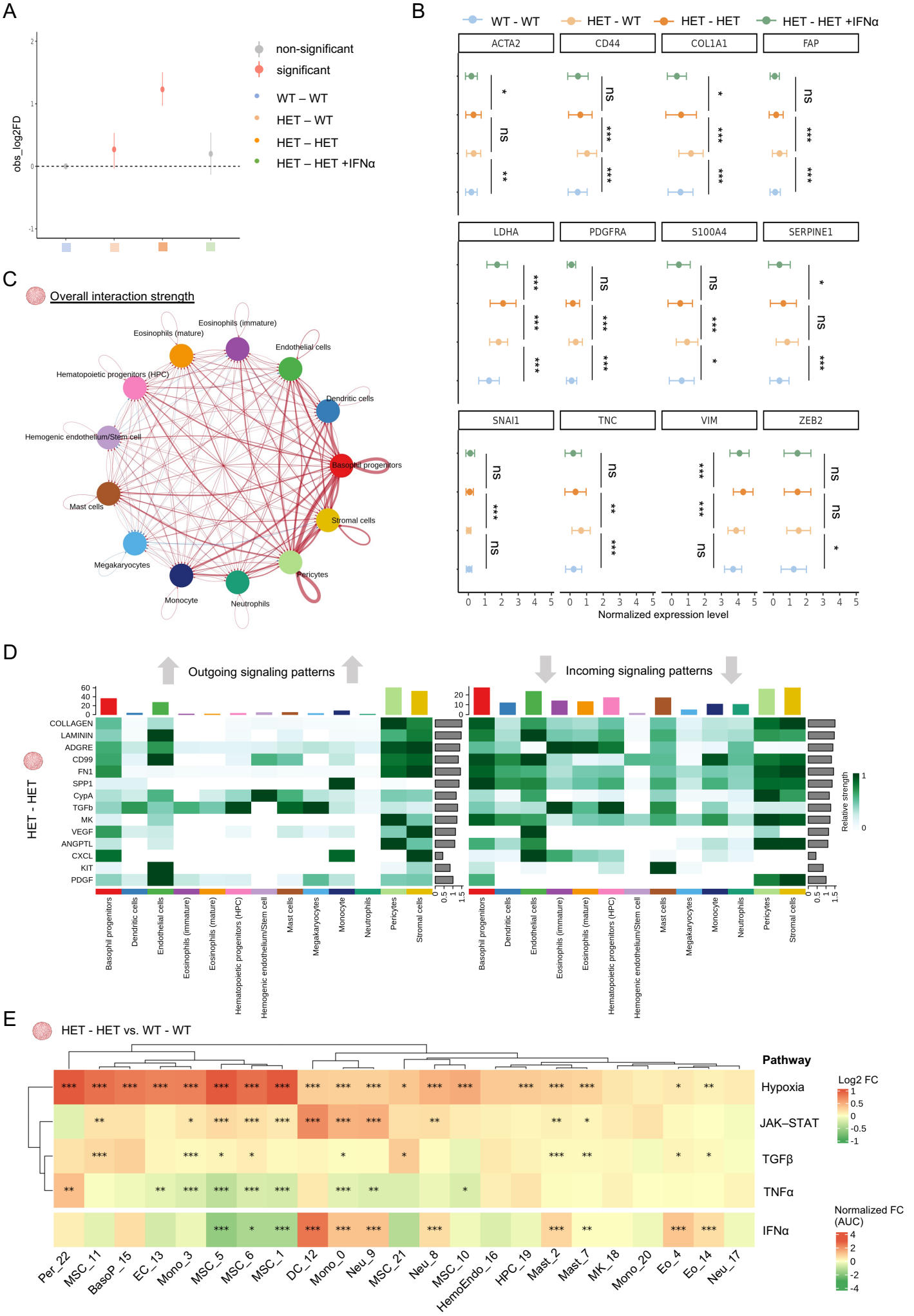
A
obs_log2FD
non-significant
significant
WT – WT
HET – WT
HET – HET
HET – HET +IFNα
B
WT - WT
HET - WT
HET - HET
HET - HET +IFNα
ACTA2
CD44
COL1A1
FAP
LDHA
PDGFRA
S100A4
SERPINE1
SNAI1
TNC
VIM
ZEB2
Normalized expression level
C
Overall interaction strength
Eosinophils (immature)
Eosinophils (mature)
Endothelial cells
Hematopoietic progenitors (HPC)
Dendritic cells
Hemogenic endothelium/Stem cell
Basophil progenitors
Mast cells
Stromal cells
Megakaryocytes
Pericytes
Monocyte
Neutrophils
D
Outgoing signaling patterns
Incoming signaling patterns
HET - HET
COLLAGEN
LAMININ
ADGRE
CD99
FN1
SPP1
CypA
TGFb
MK
VEGF
ANGPTL
CXL
KIT
PDGF
Relative strength
E
HET - HET vs. WT - WT
Pathway
Hypoxia
JAK–STAT
TGFβ
TNFα
IFNα
Log2 FC
Normalized FC (AUC)
Per_22
MSC_11
BasoP_15
EC_13
Mono_3
MSC_5
MSC_6
MSC_1
DC_12
Mono_0
Neu_9
MSC_21
Neu_8
MSC_10
HemoEndo_16
HPC_19
Mast_2
Mast_7
MK_18
Mono_20
Eo_4
Eo_14
Neu_17

Fig.4

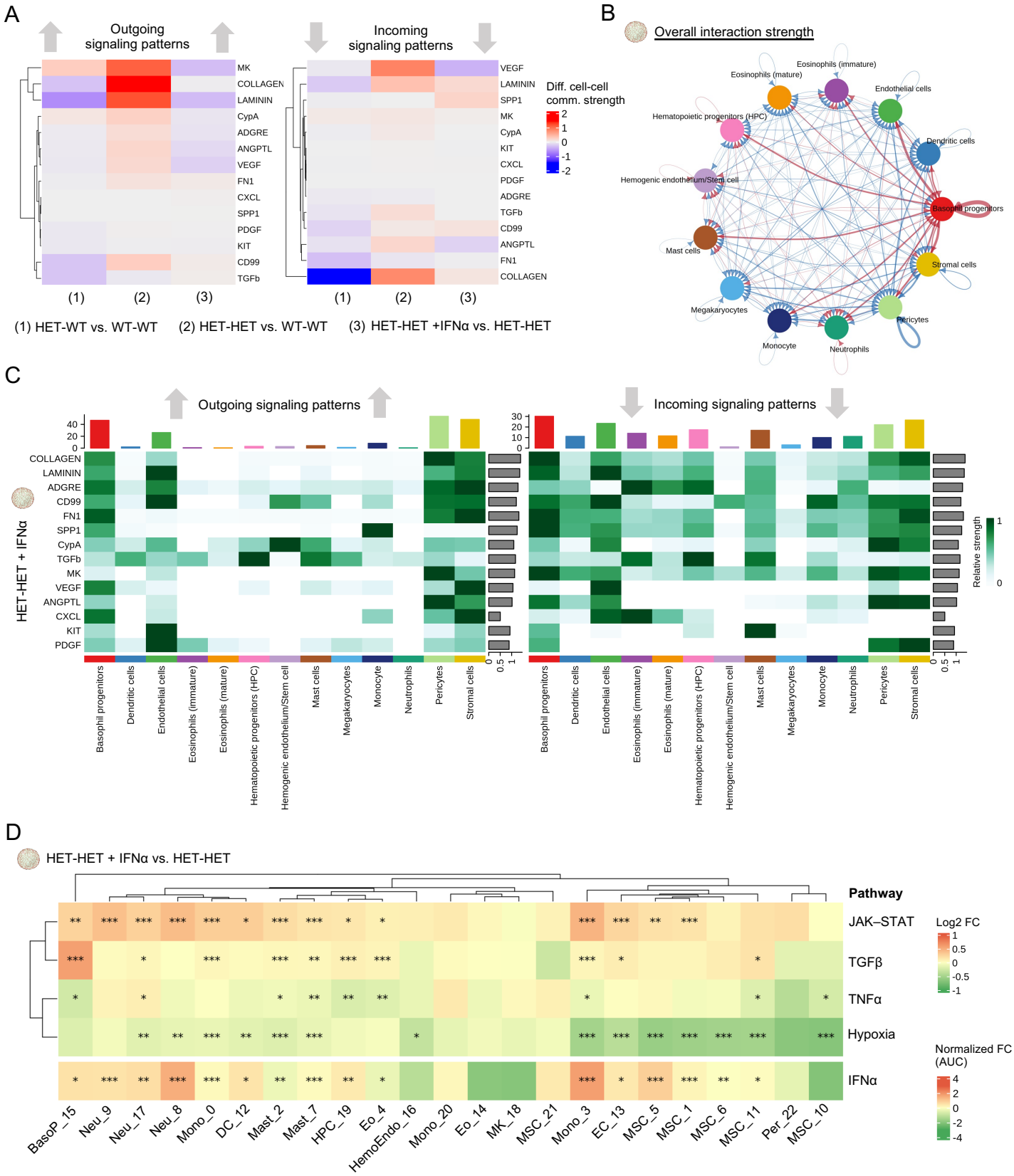
A
Outgoing signaling patterns
Incoming signaling patterns
MK
COLLAGEN
LAMININ
CypA
ADGRE
ANGPTL
VEGF
FN1
CXCL
SPP1
PDGF
KIT
CD99
TGFb
VEGF
LAMININ
SPP1
MK
CypA
KIT
CXCL
PDGF
ADGRE
TGFb
CD99
ANGPTL
FN1
COLLAGEN
Diff. cell-cell comm. strength
2
1
0
-1
-2
(1)
(2)
(3)
(1) HET-WT vs. WT-WT
(2) HET-HET vs. WT-WT
(3) HET-HET +IFNα vs. HET-HET
B
Overall interaction strength
Eosinophils (immature)
Eosinophils (mature)
Endothelial cells
Hematopoietic progenitors (HPC)
Dendritic cells
Hemogenic endothelium/Stem cell
Basophil progenitors
Mast cells
Stromal cells
Megakaryocytes
Pericytes
Monocyte
Neutrophils
C
Outgoing signaling patterns
Incoming signaling patterns
HET-HET + IFNα
COLLAGEN
LAMININ
ADGRE
CD99
FN1
SPP1
CypA
TGFb
MK
VEGF
ANGPTL
CXCL
KIT
PDGF
Relative strength
1
0
Basophil progenitors
Dendritic cells
Endothelial cells
Eosinophils (immature)
Eosinophils (mature)
Hematopoietic progenitors (HPC)
Hemogenic endothelium/Stem cell
Mast cells
Megakaryocytes
Monocyte
Neutrophils
Pericytes
Stromal cells
D
HET-HET + IFNα vs. HET-HET
Pathway
JAK–STAT
TGFβ
TNFα
Hypoxia
IFNα
Log2 FC
1
0.5
0
-0.5
-1
Normalized FC (AUC)
4
2
0
-2
-4
BasoP_15
Neu_9
Neu_17
Neu_8
Mono_0
DC_12
Mast_2
Mast_7
HPC_19
Eo_4
HemoEndo_16
Mono_20
Eo_14
MK_18
MSC_21
Mono_3
EC_13
MSC_5
MSC_1
MSC_6
MSC_11
Per_22
MSC_10

Fig. 5

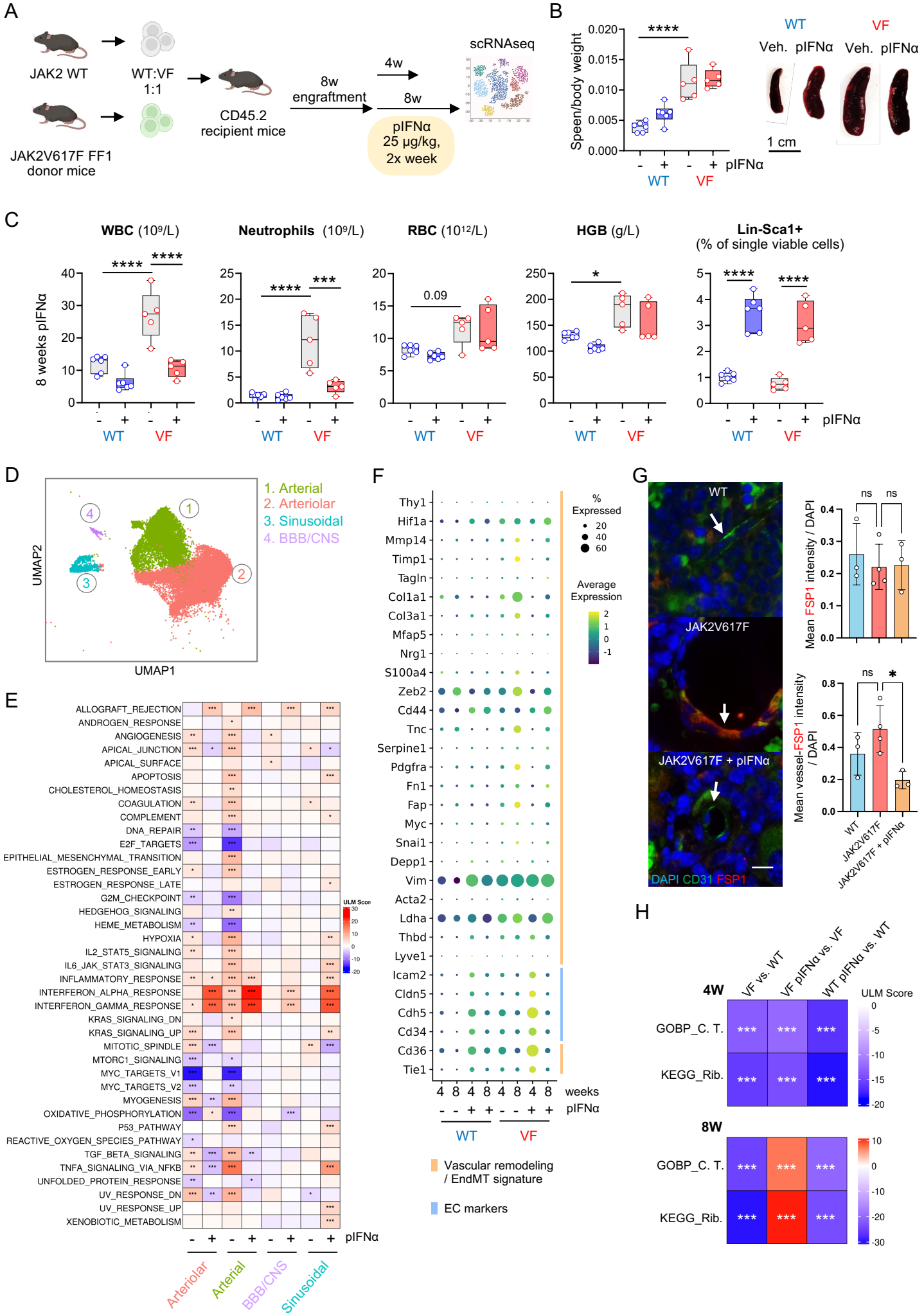
A
JAK2 WT
WT:VF 1:1
JAK2V617F FF1 donor mice
CD45.2 recipient mice
8w engraftment
4w
8w
pIFNα 25 µg/kg, 2x week
scRNAseq
B
Speen/body weight
****
WT
VF
Veh. pIFNα Veh. pIFNα
1 cm
pIFNα
C
WBC (10⁹/L)
Neutrophils (10⁹/L)
RBC (10¹²/L)
HGB (g/L)
Lin-Sca1+ (% of single viable cells)
8 weeks pIFNα
0.09
D
1. Arterial
2. Arteriolar
3. Sinusoidal
4. BBB/CNS
UMAP1
UMAP2
E
ULM Score
pIFNα
Arteriolar
Arterial
BBB/CNS
Sinusoidal
F
% Expressed
Average Expression
weeks
pIFNα
Vascular remodeling / EndMT signature
EC markers
G
WT
JAK2V617F
JAK2V617F + pIFNα
DAPI CD31 FSP1
Mean FSP1 intensity / DAPI
Mean vessel-FSP1 intensity / DAPI
ns
H
4W
8W
VF vs. WT
VF pIFNα vs. VF
WT pIFNα vs. WT
GOBP_C. T.
KEGG_Rib.
ULM Score

Fig. 6

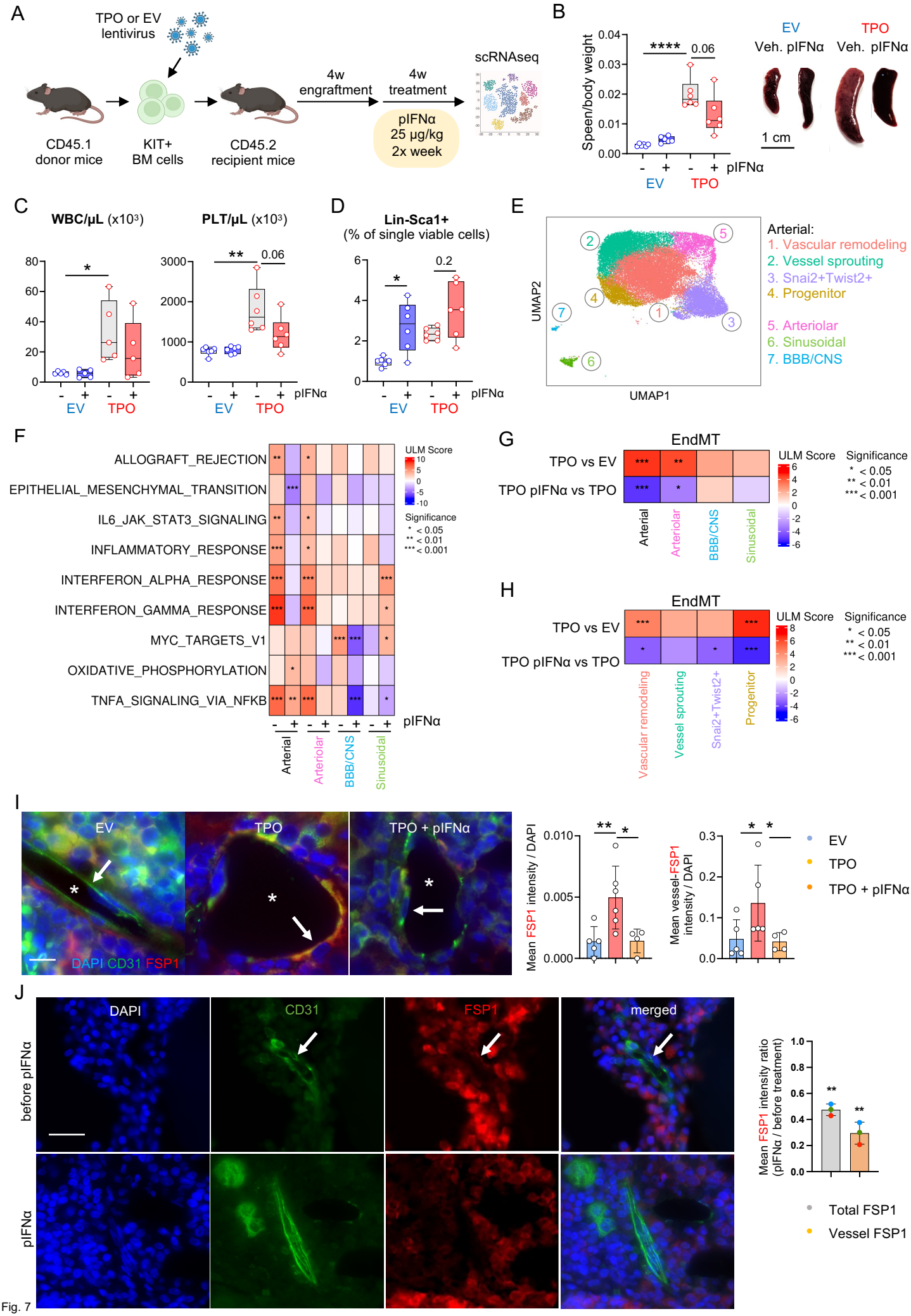
A
TPO or EV lentivirus
CD45.1 donor mice
KIT+ BM cells
CD45.2 recipient mice
4w engraftment
4w treatment
pIFNα 25 µg/kg 2x week
scRNAseq
B
Speen/body weight
****
0.06
pIFNα
EV
TPO
Veh. pIFNα
1 cm
C
WBC/µL (x10³)
PLT/µL (x10³)
D
Lin-Sca1+ (% of single viable cells)
E
UMAP2
UMAP1
Arterial:
1. Vascular remodeling
2. Vessel sprouting
3. Snai2+Twist2+
4. Progenitor
5. Arteriolar
6. Sinusoidal
7. BBB/CNS
F
ALLOGRAFT_REJECTION
EPITHELIAL_MESENCHYMAL_TRANSITION
IL6_JAK_STAT3_SIGNALING
INFLAMMATORY_RESPONSE
INTERFERON_ALPHA_RESPONSE
INTERFERON_GAMMA_RESPONSE
MYC_TARGETS_V1
OXIDATIVE_PHOSPHORYLATION
TNFA_SIGNALING_VIA_NFKB
ULM Score
Significance
Arterial
Arteriolar
BBB/CNS
Sinusoidal
G
EndMT
TPO vs EV
TPO pIFNα vs TPO
H
Vascular remodeling
Vessel sprouting
Snai2+Twist2+
Progenitor
I
EV
TPO
TPO + pIFNα
DAPI CD31 FSP1
Mean FSP1 intensity / DAPI
Mean vessel-FSP1 intensity / DAPI
J
DAPI
CD31
FSP1
merged
before pIFNα
pIFNα
Mean FSP1 intensity ratio (pIFNα / before treatment)
Total FSP1
Vessel FSP1

Fig. 7

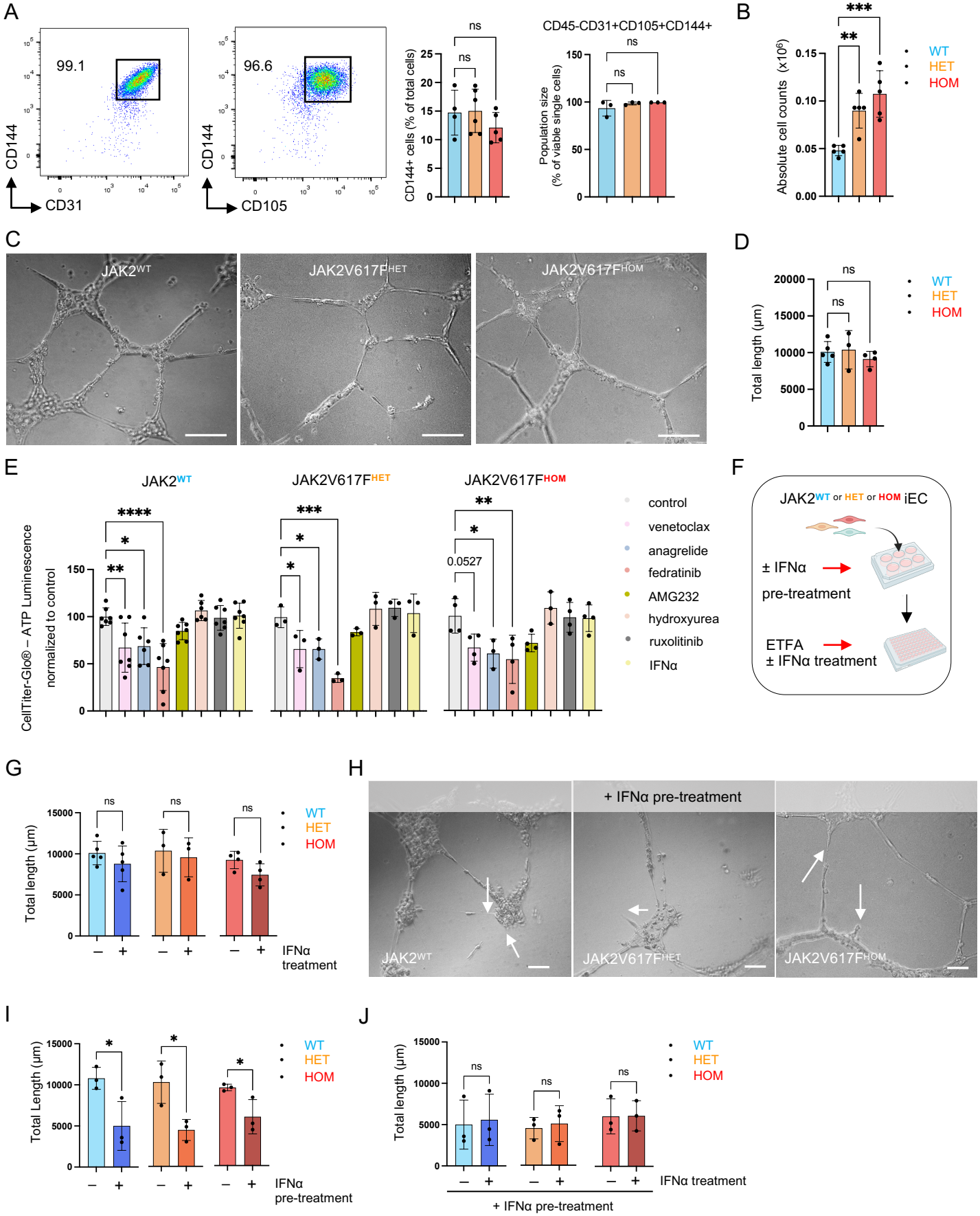

Supplemental Fig. 1

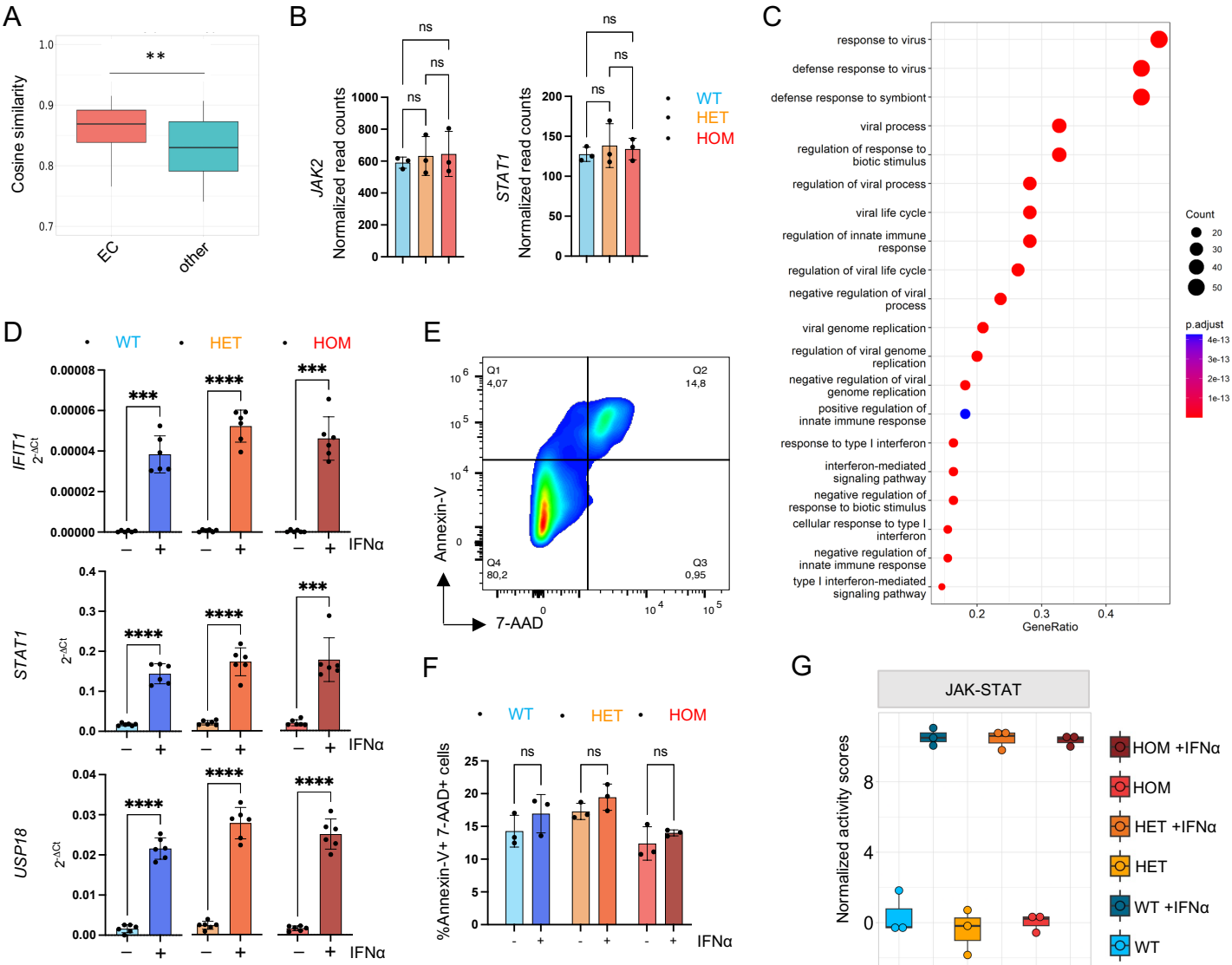

Supplemental Fig. 2

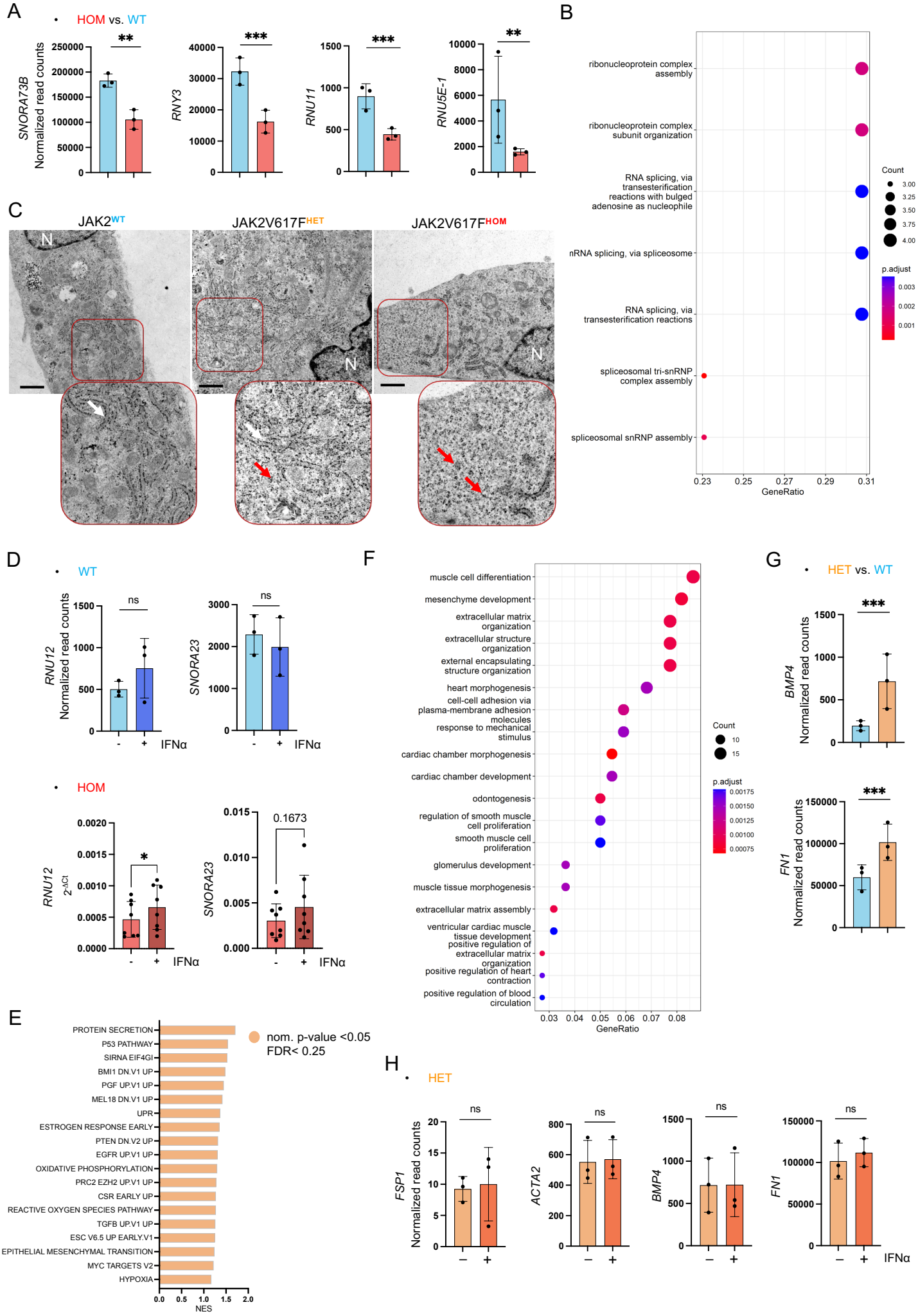

Supplemental Fig. 3

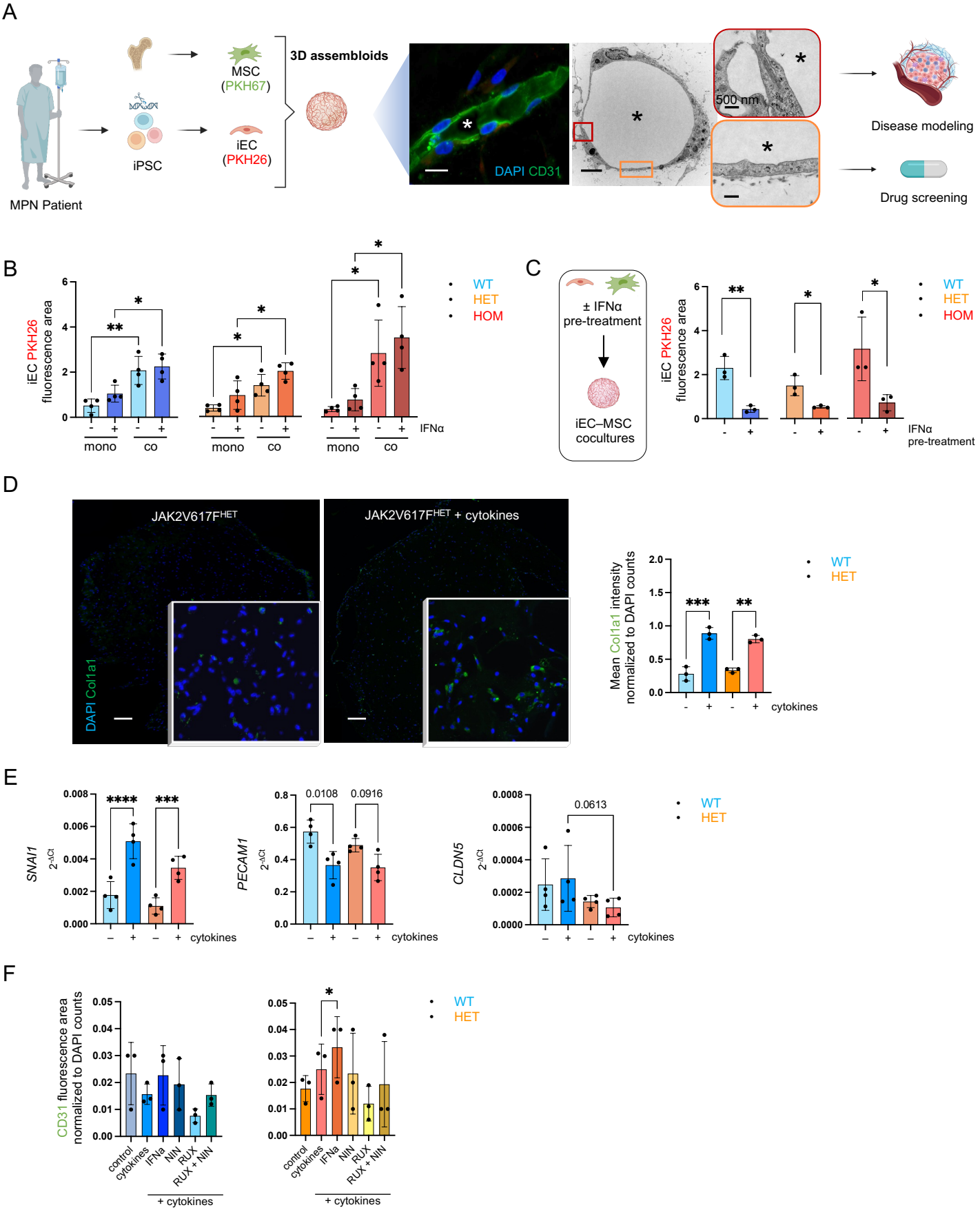

Supplemental Fig. 4

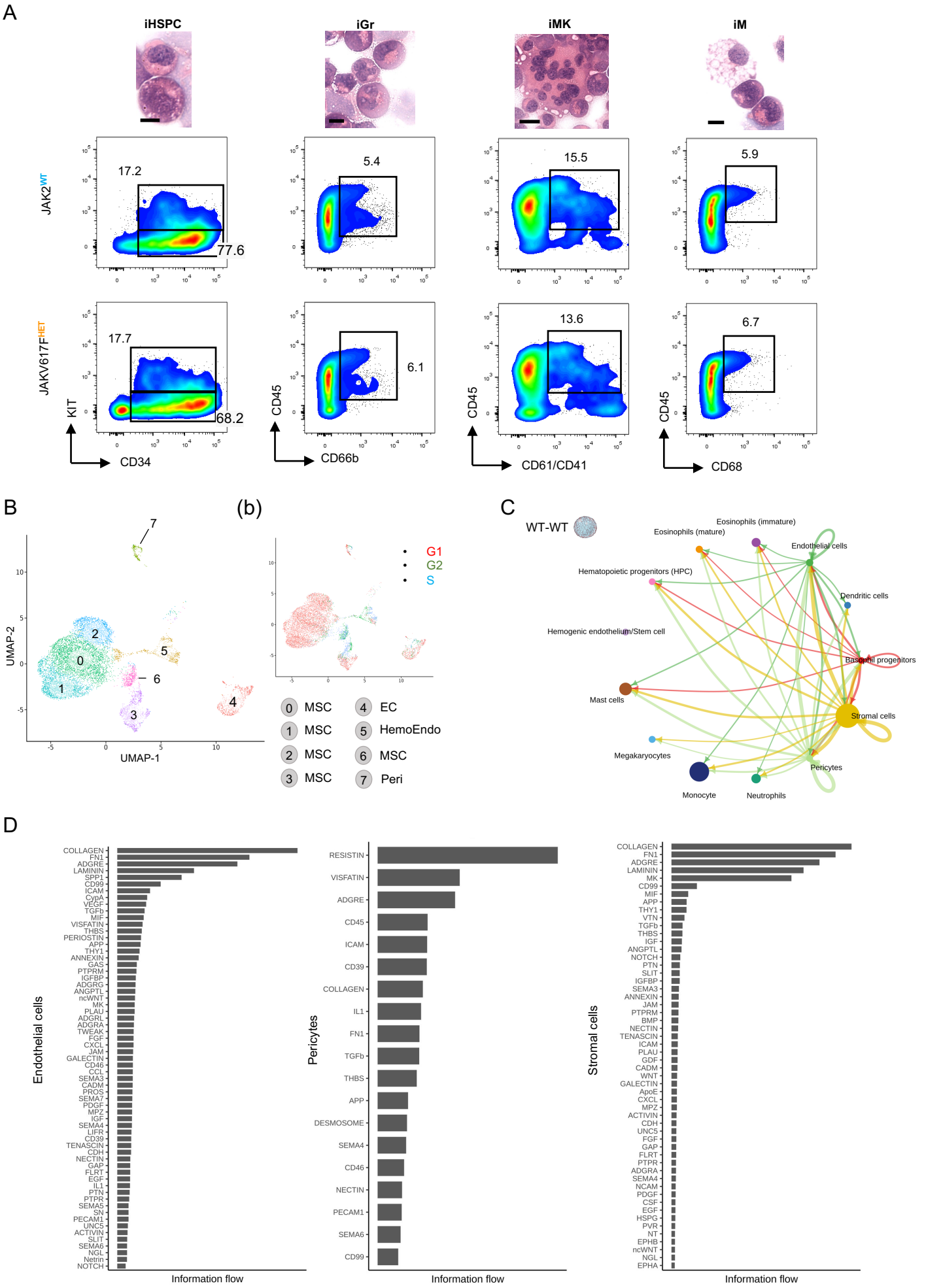

Supplemental Fig. 5

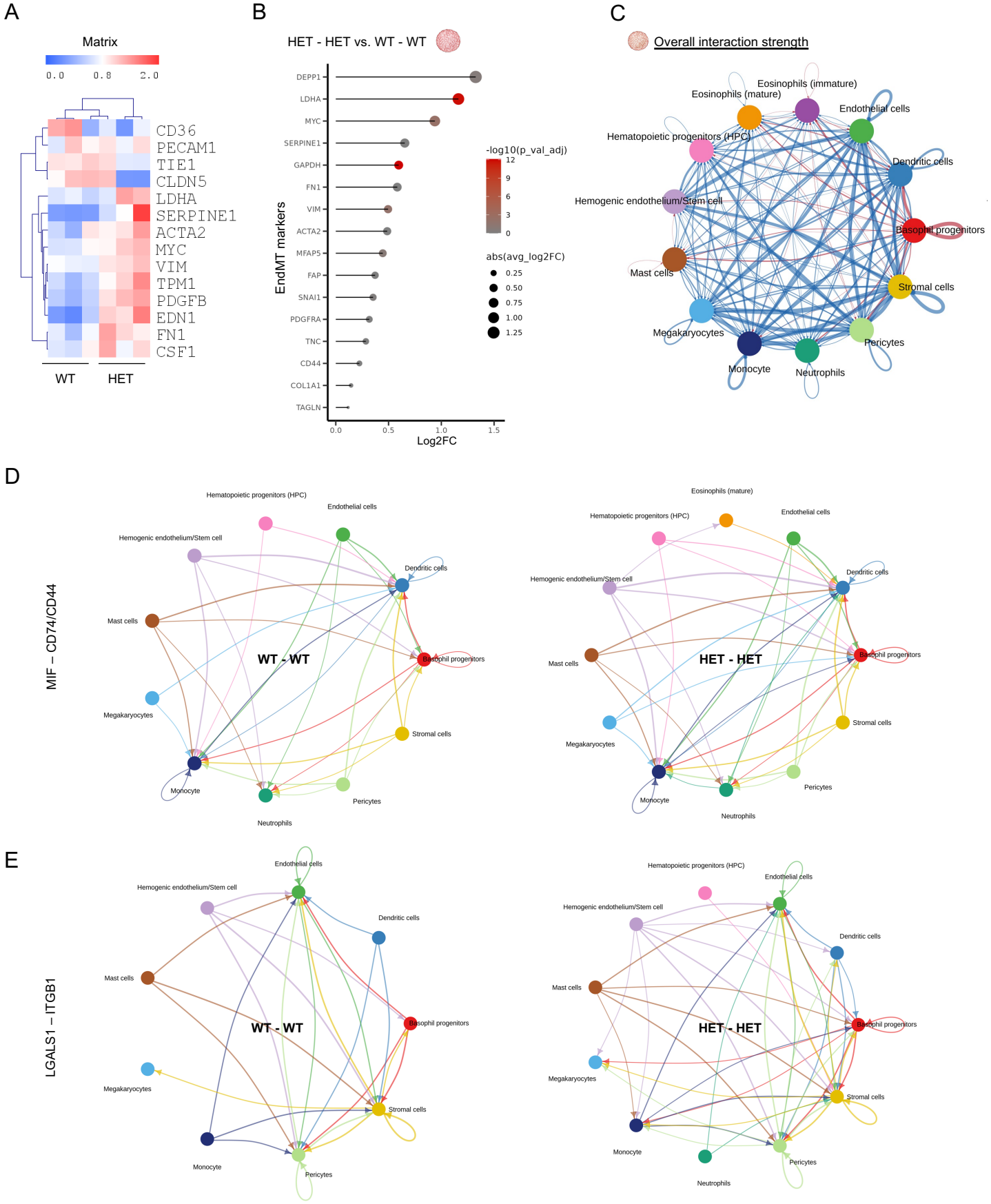

Supplemental Fig. 6

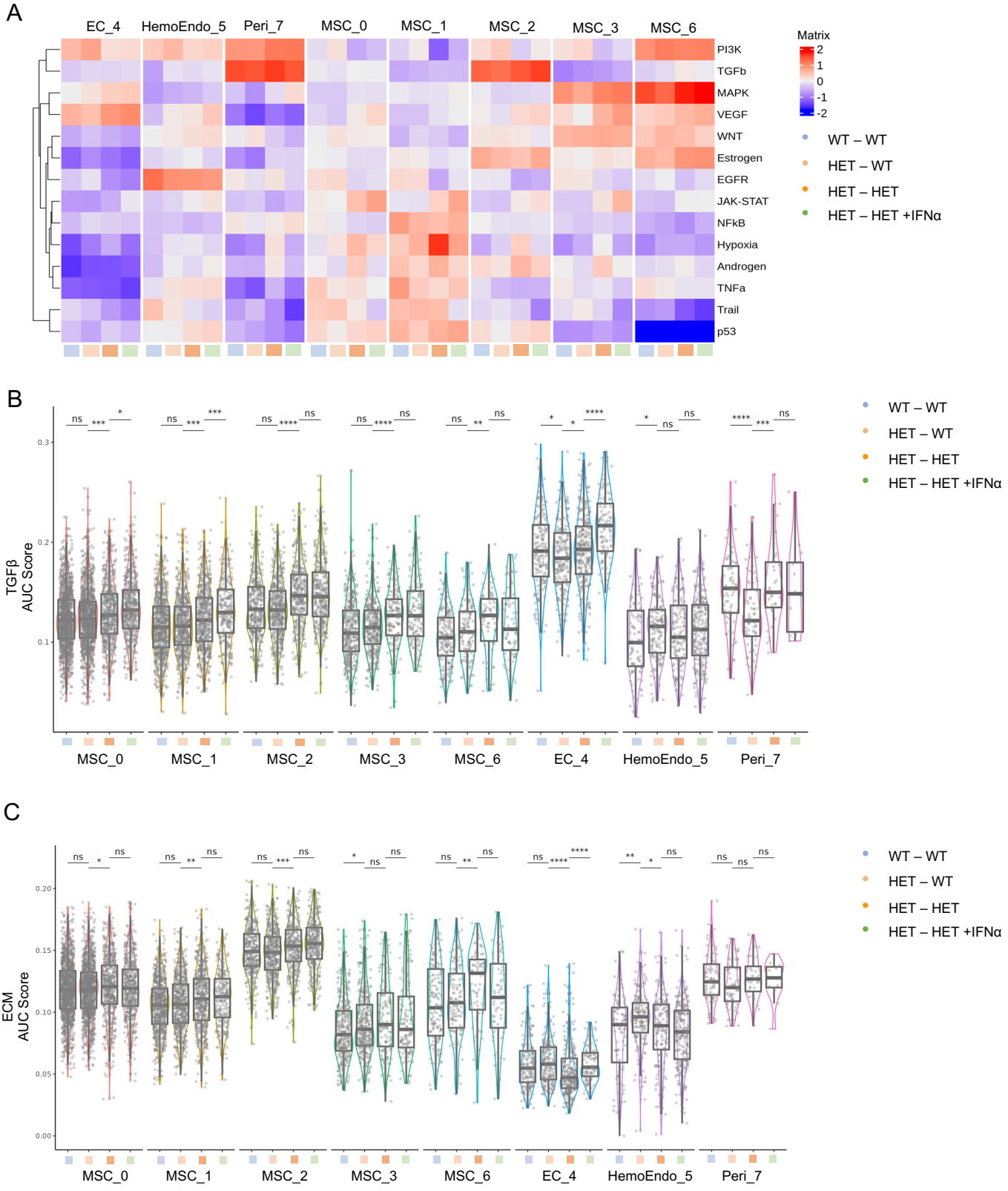

Supplemental Fig. 7

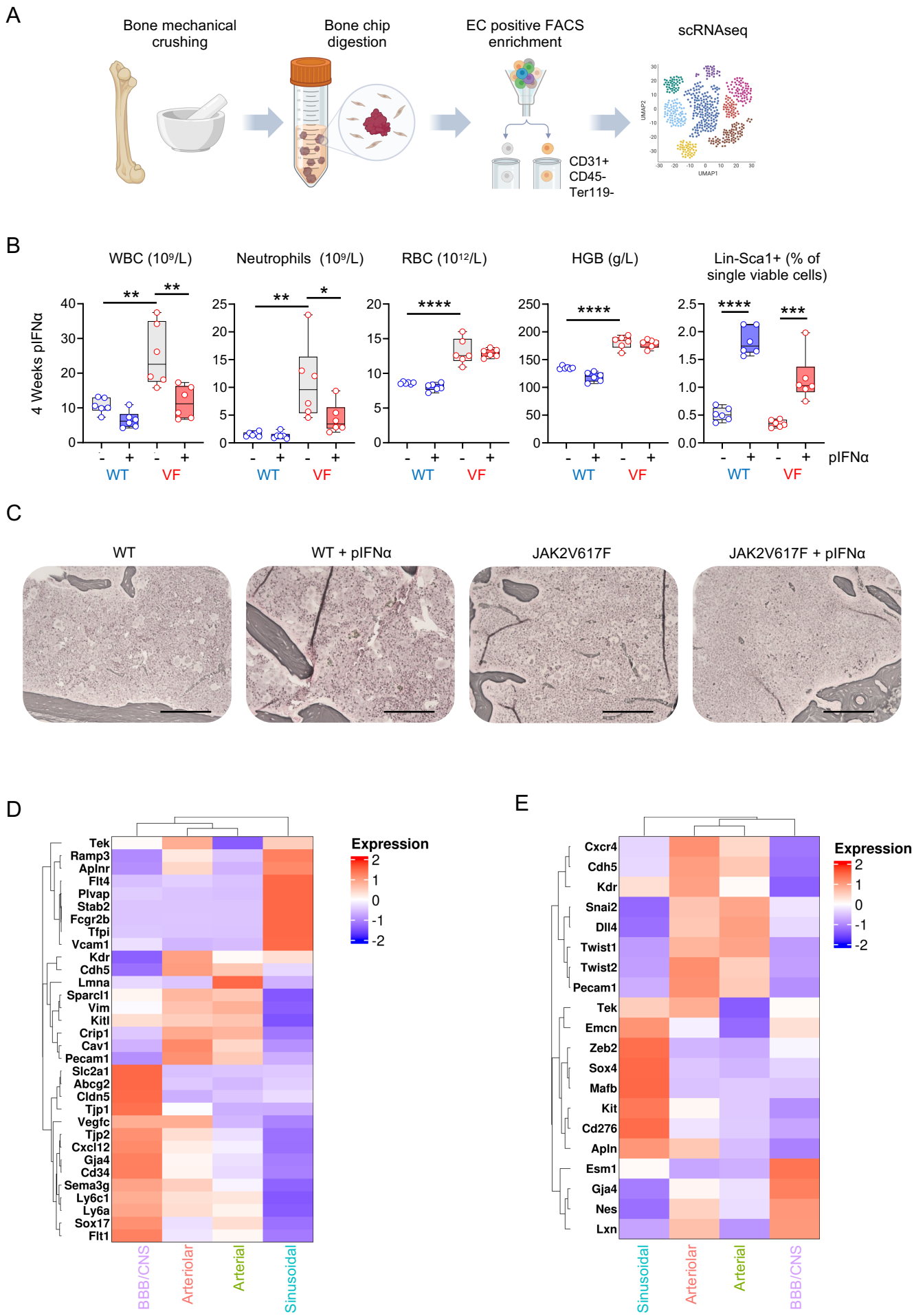

Supplemental Fig. 8

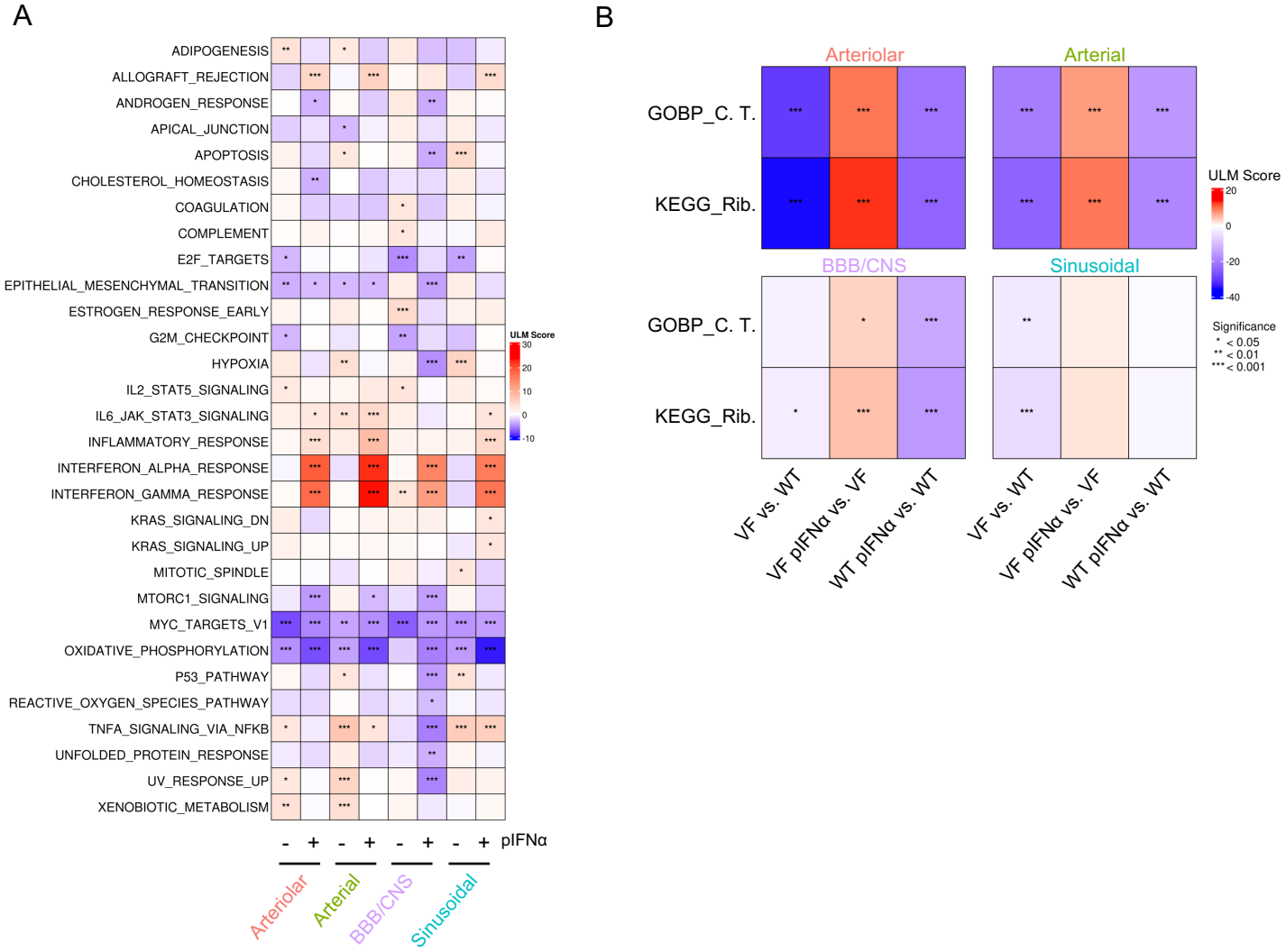

Supplemental Fig. 9

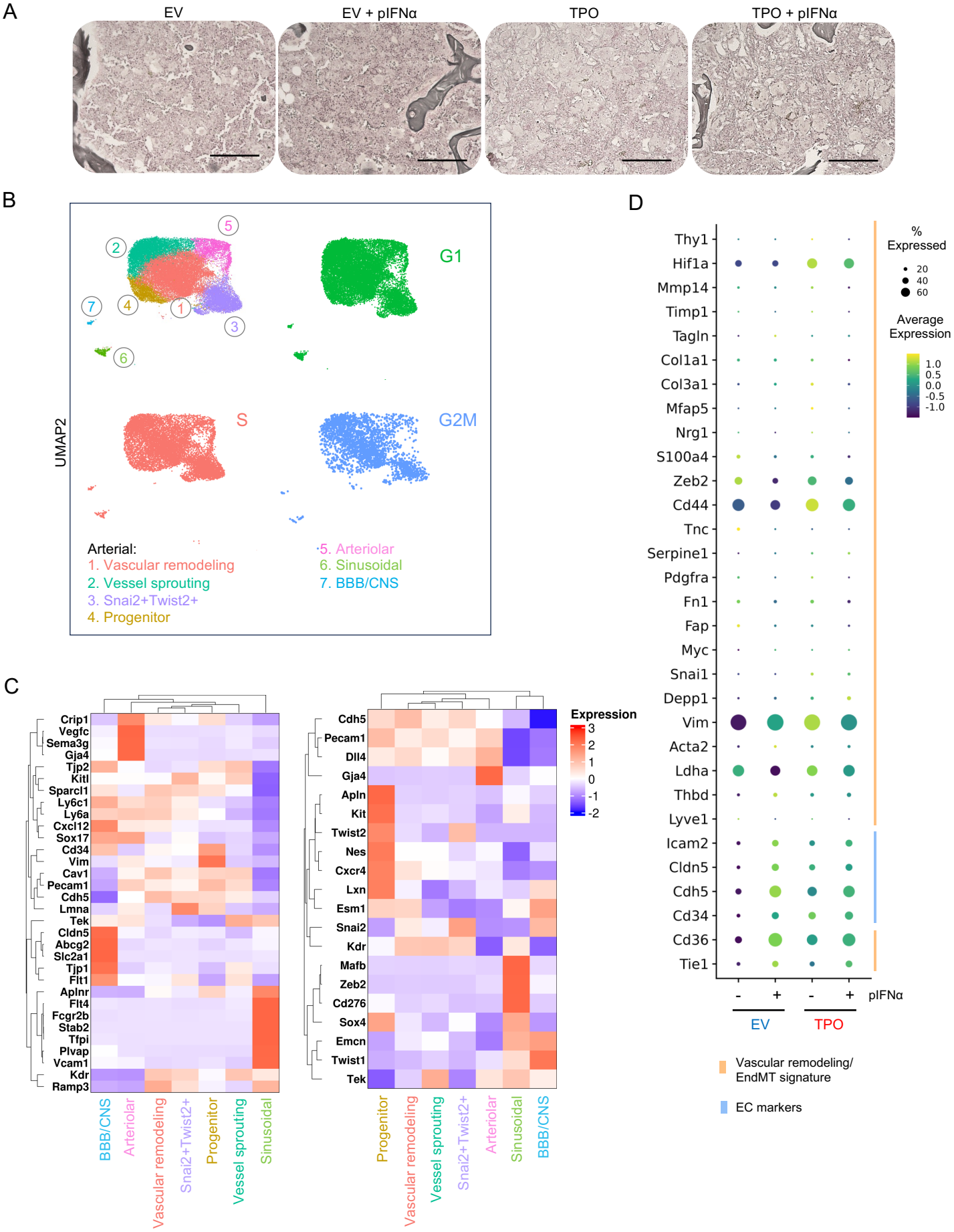

Supplemental Fig. 10